Partitioning global land evapotranspiration using CMIP5 models constrained by observations

Xu Lian, Shilong Piao, Chris Huntingford, Yue Li, Zhenzhong Zeng, Xuhui Wang, Philippe Ciais, Tim Mcvicar, Shushi Peng, Catherine Ottle, et al.

Partitioning global land evapotranspiration using CMIP5 models constrained by observations

Xu Lian[1], Shilong Piao[1,2,3*], Chris Huntingford[4], Yue Li[1], Zhenzhong Zeng[1], Xuhui Wang[1], Philippe Ciais[5], Tim R. McVicar[6,7], Shushi Peng[1], Catherine Ottlé[5], Hui Yang[1], Yuting Yang[8], Yongqiang Zhang[6] and Tao Wang[2,3]

The ratio of plant transpiration to total terrestrial evapotranspiration (T/ET) captures the role of vegetation in surface–atmo-sphere interactions. However, its magnitude remains highly uncertain at the global scale. Here we apply an emergent constraint approach that integrates CMIP5 Earth system models (ESMs) with 33 field T/ET measurements to re-estimate the global T/ET value. Our observational constraint strongly increases the original ESM estimates (0.41± 0.11) and greatly alleviates intermodel discrepancy, which leads to a new global T/ET estimate of 0.62± 0.06. For all the ESMs, the leaf area index is iden-tified as the primary driver of spatial variations of T/ET, but to correct its bias generates a larger T/ET underestimation than the original ESM output. We present evidence that the ESM underestimation of T/ET is, instead, attributable to inaccurate representation of canopy light use, interception loss and root water uptake processes in the ESMs. These processes should be prioritized to reduce model uncertainties in the global hydrological cycle.

Terrestrial evapotranspiration (ET) is a key component of the global hydrological cycle and also represents a central link-age with the surface energy balance and carbon cycle[1–3]. Two separate processes together constitute this flux, namely physical evaporation (that is, soil and inland water evaporation and canopy interception loss) and biological transpiration (T)[3]. Both processes respond differently to changes in surface meteorological conditions, soil moisture status and vegetation abundance[4]. To quantify the ratio of transpiration to ET (that is, T/ET) is accordingly necessary to estimate accurately the land water fluxes across spatial scales, and eventually provides insights into global interactions between terrestrial ecosystems and the atmosphere[5,6]. As the biological processes that influence T also control land–atmosphere carbon dioxide exchanges, more accurate T/ET estimates aid global carbon cycle projections. Over the past decade, considerable efforts have been made to improve our knowledge of T/ET, but its value is still subject to debate[1,7–16]. For instance, one extrapolation of isotope-based catchment-scale estimates to a global scale[1] suggested that global T/ET was as high as 0.80–0.90, although this may be an overestimate[14–16]. A smaller T/ET estimate of 0.64 ± 0.13 (mean ± s.d.) was reported more recently[8], based on the global water-isotope budget. The difference between the two water-isotope-based global ET partitioning studies[1,8] derives mostly from their inclusion of different canopy interception values[10]; both imply transpiration fluxes that exceed soil and lake evaporation fluxes[10].

Site measurements provide accurate local information on the T/ET ratio, but are limited by their relative scarcity and inconsistent measurement periods (from only a few days or months up to years, depending on the location). This precludes large-scale upscaling, for example, using empirical statistical models based on environmental variables such as the leaf area index (LAI)-based regression[10]. Alternatively, Earth system models (ESMs) offer an effective way to derive T/ET estimates across temporal and spatial scales. The approach taken is that ESMs are first proved to perform well in reproducing T/ET at single points with the available measurements. Then, an assumption is made that they capture accurately the spatial variations in the present or future surface climate conditions that force T/ET, which enables aggregation up to the global scale. ESMs are routinely used to assess evaporation and water resource changes in response to rising atmospheric greenhouse gas concentrations[17–19], as well as feedbacks of an adjusted hydrological cycle to the climate system[6]. However, different ESMs inevitably produce divergent T/ET estimates because they contain diverse parameterizations of surface energy and water processes from alternative strands of development in the past few decades. Here we use historical outputs from 19 ESMs (Methods and Supplementary Table 1) under the Climate Model Intercomparison Project Phase 5 (CMIP5)[20] for the period 1980–2005 (Fig. 1a), together with 33 site observations of the annual average T/ET compiled from field-based studies that cover at least a full year (Fig. 1a,c) to derive a reassessment of the global T/ET magnitude.

Evaluating model performance

We first compared T/ET in CMIP5 models against five existing global-scale estimates[1,4,7–10] and against 33 direct site observations, which are a mixture of isotopic and non-isotopic measurements (Methods and Supplementary Table 2). The T/ET of most ESMs exhibits a consistent tendency towards maximizing in the tropics and decreasing poleward, although at all latitudes the magnitude of present-day T/ET varies considerably across ESMs (Fig. 1b).

[1]Sino-French Institute for Earth System Science, College of Urban and Environmental Sciences, Peking University, Beijing, China. [2]Key Laboratory of Alpine Ecology and Biodiversity, Institute of Tibetan Plateau Research, Chinese Academy of Sciences, Beijing, China. [3]Center for Excellence in Tibetan Earth Science, Chinese Academy of Sciences, Beijing, China. [4]Centre for Ecology and Hydrology, Wallingford, UK. [5]Laboratoire des Sciences du Climat et de l'Environnement (LSCE), CEA CNRS UVSQ, Gif Sur Yvette, France. [6]CSIRO Land and Water, Canberra, Australian Capital Territory, Australia. [7]Australian Research Council Centre of Excellence for Climate System Science, Sydney, New South Wales, Australia. [8]State Key Laboratory of Hydro-Science and Engineering, Department of Hydraulic Engineering, Tsinghua University, Beijing, China. *e-mail: slpiao@pku.edu.cn

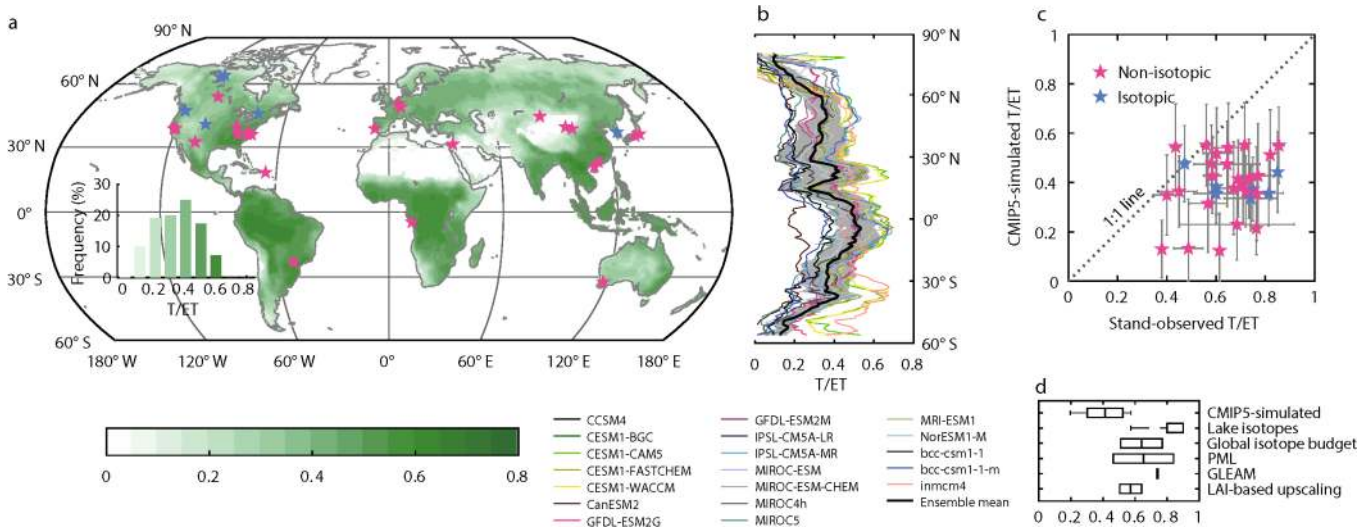

Fig. 1 Simulated and observation-based estimates of T/ET at the global and stand levels. a, Spatial pattern (map) and corresponding frequency distribution (inset) of the CMIP5 ensemble mean T/ET for the period 1980–2005. Stars indicate the locations of sites that provided stand-level observations for this study. **b**, Latitudinal profiles of ESM-modelled T/ET; the grey shading indicates the uncertainty range (mean ± s.d.). **c**, Scatterplot of the site-observed T/ET versus the mean modelled T/ET extracted for the same locations. Error bars represent the uncertainty range of ESM simulations (vertical) and of the field observations (horizontal). **d**, Global average T/ET estimates from different sources; boxes mark the given uncertainty range[1,4,7–10], bold black lines mark the mean values and error bars indicate the maximum/minimum values.

Averaged globally, intermodel discrepancies span a factor of about three (from 0.20 in CanESM2 to 0.57 in CESM1-CAM5). Critically, the multiyear average of the CMIP5 model ensemble mean (0.41 ± 0.11) is considerably lower than all the observation-based estimates derived from lake isotopes[1,7] (0.57–0.90), from global water isotope budgets[8] (0.64 ± 0.13), from the Penman–Monteith–Leuning (PML) model[4] (0.65 ± 0.19), from the Global Land Evaporation Amsterdam Model[9] (GLEAM, 0.74) and from LAI-based upscaling[10] (0.57 ± 0.07) (Fig. 1d). To further verify that CMIP5 models underestimate T/ET, we also compared model simulations with local field observations, after sampling the models at grid cells that contain each site. As discovered at the global scale, modelled T/ET is substantially lower (six out of seven sites) than isotopic measurements by an average of 46%, and lower (24 out of 26 sites) than non-isotopic measurements by an average of 36% (Fig. 1c). Among the three sites with lower field observations of T/ET than model estimates, they are only on average 5% less than the CMIP5-mean ensemble for those locations.

New global T/ET estimate constrained by observations

To build the usefulness of ESM-based global estimates of T/ET, we made use of these field T/ET measurements through an emergent constraint approach (Methods). This approach can lever additional information from a multimodel ensemble to reduce the uncertainty in characterizing Earth system features (for example, Cox et al.[21], Mystakidis et al.[22] and Wenzel at al.[23]). The concept relies on the fact that, although ESMs may have many large intermodel structural and parameter differences, there may exist a tight regression across them between (1) a quantity of interest that is difficult to measure and (2) a second variable for which measurement data are readily available. Applying this approach here, a tight linear relationship across ESMs ($R^2 = 0.93$, $P < 0.001$ (Fig. 2a)) was found between the modelled global T/ET values (areal-averaged global T divided by areal-averaged global ET) and the modelled site-averaged T/ET (T/ET averaged over the grid cells that correspond to the observational site locations) for the contemporary period (1980–2005). This strong linear relationship between individual model simulations of site-average T/ET for the contemporary period and their estimates of global T/ET provides an emergent constraint on the actual global T/ET value—that is, by using the regression to map from site-average T/ET measurements (Fig. 2a). Our summary result shows that the constrained global T/ET ratio of 0.62 ± 0.06 is 34% higher than that of the original CMIP5 ensemble mean (that is, 0.41 ± 0.11), with a reduction in the uncertainty range by nearly half (Fig. 2b). Additional statistical and sensitivity analyses were performed that confirm the robustness of this higher global T/ET value than the original model output (Methods and Supplementary Figs. 1–3). As isotopic approaches often diagnose higher T/ET values than other approaches[7,11], the global re-estimate of T/ET constrained by isotopic observations only (0.71 ± 0.07) is larger than that constrained by non-isotopic observations only (0.60 ± 0.06) (Supplementary Fig. 4).

Drivers of spatial variation in modelled T/ET

ET partitioning is highly dependent on land surface properties (for example, vegetation density and structure[10,24] and soil moisture[15]) and atmospheric conditions (for example, energy availability[15] and precipitation (PRE) characteristics). To aid our understanding of the T/ET model bias, we investigated the dominant drivers of spatial gradients of T/ET in different CMIP5 models. We developed an empirical diagnostic model for offline T/ET estimates as a function of 14 environmental factors (Supplementary Table 3). This diagnostic model is based on boosted regression trees (BRTs (Methods)), a machine-learning technique extended from traditional classification and regression trees. The BRT model based on these factors successfully explains 95–99% of the global spatial patterns of T/ET in all the 19 ESMs considered. Figure 3 displays the amount of spatial variation in T/ET explained by each environmental factor, and for each ESM. LAI is identified as the primary driver of T/ET for all the 19 CMIP5 ESMs—its relative contribution to explaining the spatial patterns of T/ET varies from 25 to 86% (Fig. 3) and, for all individual models, has the highest percentage compared to that of other factors. This verifies the critical role of the terrestrial vegetation structure in controlling ET partitioning[10,24]. There is no cross-model consensus on the second most important driver for spatial gradients in T/ET, being either temperature (maximum

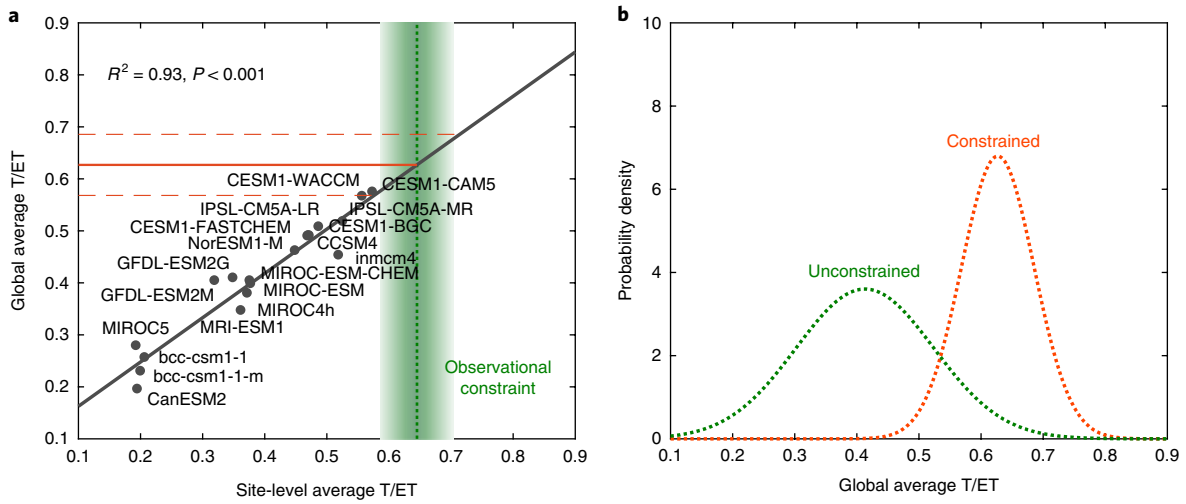

Fig. 2 Emergent constraint on the model-simulated global T/ET. a, Global average T/ET versus the simulated cross-site average T/ET based on observational site locations for the 19 CMIP5 ESMs. The grey line indicates the best-fit regression line across the models. The green dashed line (stand-level average T/ET) and shaded areas (uncertainty range) represent the observation-based constraint on the simulated global average T/ET value. Orange lines show the constrained global T/ET (solid) and its uncertainty range (dashed). **b**, PDF for the original ESM global average T/ET (green line), and the estimated global average T/ET by applying observational constraint onto the intermodel relationship shown in **a**.

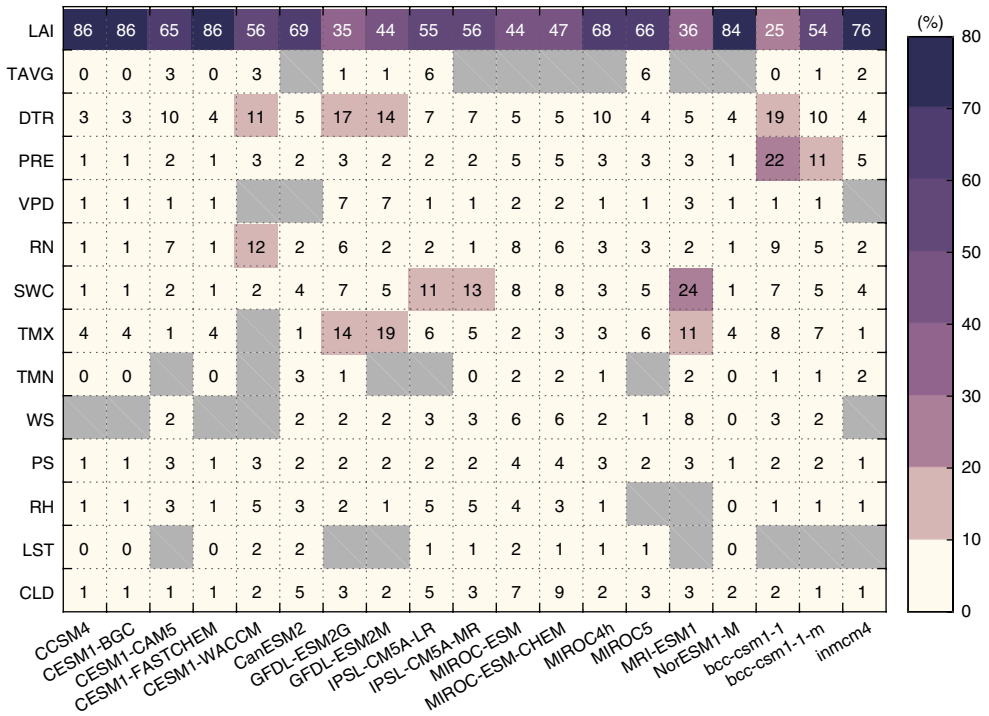

Fig. 3 Contribution of environmental drivers to spatial variations of T/ET in ESMs. Shown are the relative contributions, as integer percentages (%), of 14 environmental drivers (*y* axis (details in Supplementary Table 3)) to spatial variations of T/ET across 19 CMIP5 models (*x* axis (details in Supplementary Table 1)). Grey grids indicate that these drivers have very minor impacts on the T/ET distribution in the corresponding ESM, so they were not included in constructing BRT models (Supplementary Text 2). Altogether, all the remaining drivers in each ESM can explain at least 95% of the global spatial variation of T/ET.

air temperature (TMX) or diurnal temperature range (DTR)), water availability (PRE or soil water content (SWC)), or radiation (net radiation (RN)).

To explore whether any biases in the dominant drivers (those that explain over 10% of the total spatial variations in T/ET) cause an underestimation in the modelled T/ET, we re-ran the BRT model calibrated for each ESM, but with the dominant drivers replaced by corresponding global observations instead of ESM outputs (Methods). All the ESMs, except MIROC5 and CanESM2, overestimate LAI, with the ensemble mean LAI being approximately 1.5 times that of satellite observations (Fig. 4a). These ESMs thus project a too high T/ET because of their too high LAI values, although different models show substantially different relationships between T/ET and LAI (Fig. 4b). Accordingly, compared to the original ESM

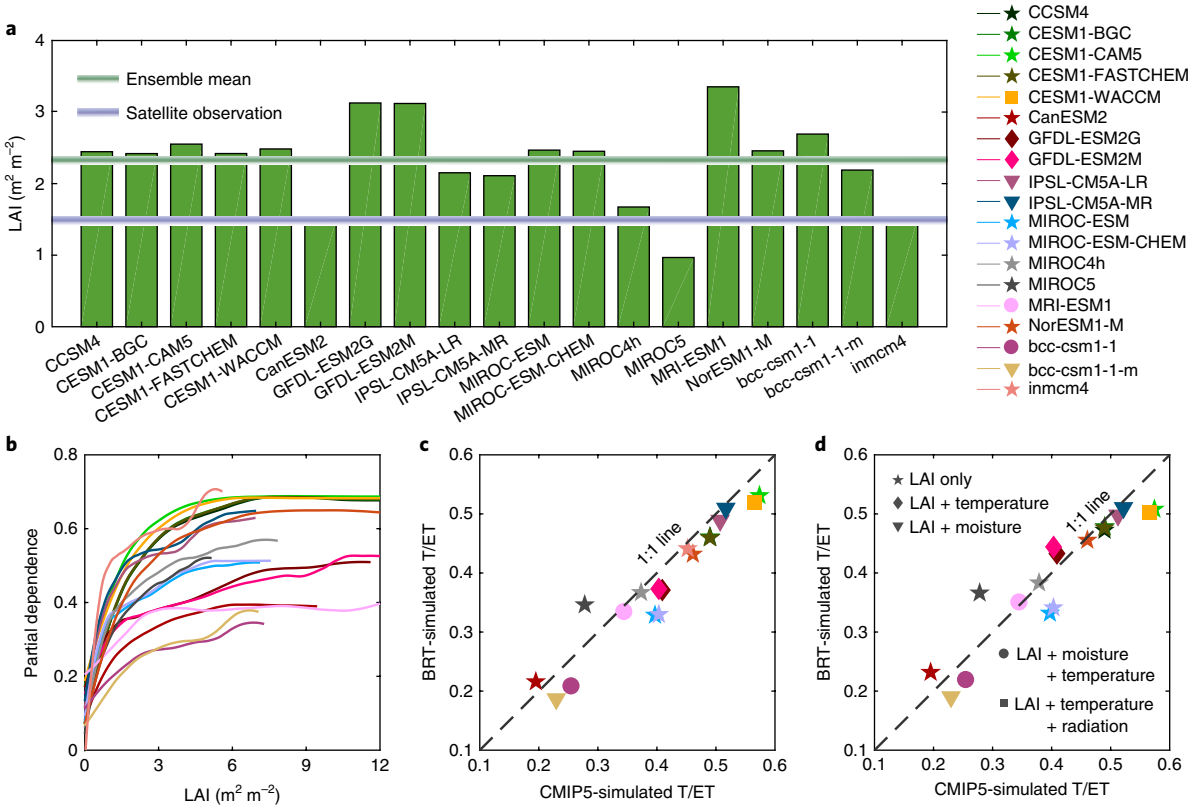

Fig. 4 | Implications for the model-derived T/ET of replacing dominant drivers with observations. a, Comparison between global-mean model-derived LAI (1980–2005) and remotely sensed LAI (1981–2005). **b**, Partial dependency plot for LAI from the BRT model built with land pixels of each CMIP5 ESM. **c**, Scatterplot of CMIP5-modelled T/ET versus BRT-modelled T/ET, but with LAI replaced by satellite observations. **d**, Scatterplot of CMIP5-modelled T/ET versus BRT-modelled T/ET with LAI, DTR, TMX, SWC, PRE and RN replaced by the corresponding observations or climate reanalysis. ESM colours are common to panels **b**–**d**. Different shapes of symbols indicate the five categories of ESM-specific dominant drivers that govern global land ET partitioning (Methods).

estimates, the predicted global T/ET driven by satellite-observed LAI actually leads to an even larger underestimation of T/ET in 17 models (from 0.01 for IPSL-CM5A-MR to 0.07 for MIROC-ESM-CHEM) (Fig. 4c). These results suggest strongly that the underestimation in ESM-simulated global T/ET is attributable to inaccurate representations of vegetation-related processes that influence ET partitioning, instead of the direct erroneous magnitude of vegetation density as represented through LAI in the ESMs. We also verify that correcting the bias of each of the dominant drivers beside LAI cannot enhance the modelled global T/ET magnitude (Supplementary Text 3 and Supplementary Fig. 5). Overall, if all the dominant drivers are replaced by observations instead of ESM variables, the global T/ET in most (13 of 19) ESMs would actually decrease (except the MIROC5, CanESM2 and the GFDL models) from the original values of 0.41 ± 0.11 to a new range of 0.38 ± 0.10 (Fig. 4d). Hence, the direct inclusion of observed driving data to recalculate the T/ET value, via the BRT model trained on ESM output, causes even larger biases.

Potential causes of the underestimation in modelled T/ET

Confirmation that biases in surface drivers, including LAI, are not responsible for the large ESM underestimation of T/ET implies that structural deficiencies exist in how ESMs partition land ET into its component fluxes. Furthermore, the strong linkage between the T/ET value and LAI (Figs. 3 and 4b) indicates that such structural errors may be dependent on physiological and within-canopy processes, whose parameterization relates to LAI. We developed an adjusted 'big-leaf' model[25,26] to approximate the photosynthesis and transpiration processes for each ESM (Supplementary Text 4). We diagnosed that the implied big-leaf light extinction coefficients (τ) currently in most ESMs (Supplementary Table 4) are generally higher than those reported from site observations[25]. Indeed, nearly two-thirds of the ESMs have values higher than the standard value of 0.5 often assumed in any big-leaf approach[26]. Accordingly, lower τ values ($\tau \leq 0.4$ based on available observations[25]) applied to each inferred model result in a substantial increase ($\geq$25%) in the ensemble mean global T/ET (Supplementary Fig. 6). The overestimated τ could be partially attributable to errors in some light-related drivers, which include the requirement for a routine inclusion of diffuse radiation—an effect shown to be important for the photosynthetic response to light[27,28]. For instance, without an explicit representation of diffuse-light dependence (except the Community Land Model version 4.0), ESMs may underestimate the transpirational ability of shaded canopy leaves under 'hazy' radiation conditions[29,30]. Although presently very limited direct in-canopy measurements are available to test for this effect, the observed substantial impact of diffuse radiation on the canopy photosynthesis[27–29] supports this hypothesis because carbon uptake and water loss are inherently coupled[1,31,32].

In addition to the possibly incorrect τ values, there is emerging evidence of an underestimation in the global light-use efficiency (LUE), which measures the ability to fix carbon per unit of photosynthetically active radiation[33]. In ESMs, LUE has a global and model mean of $0.90 \pm 0.26\,\mathrm{gC\,m^{-2}\,MJ^{-1}}$ absorbed photosynthetically active radiation (APAR) (Supplementary Text 5 and Supplementary Table 4), compared to a recent global empirical estimate based on

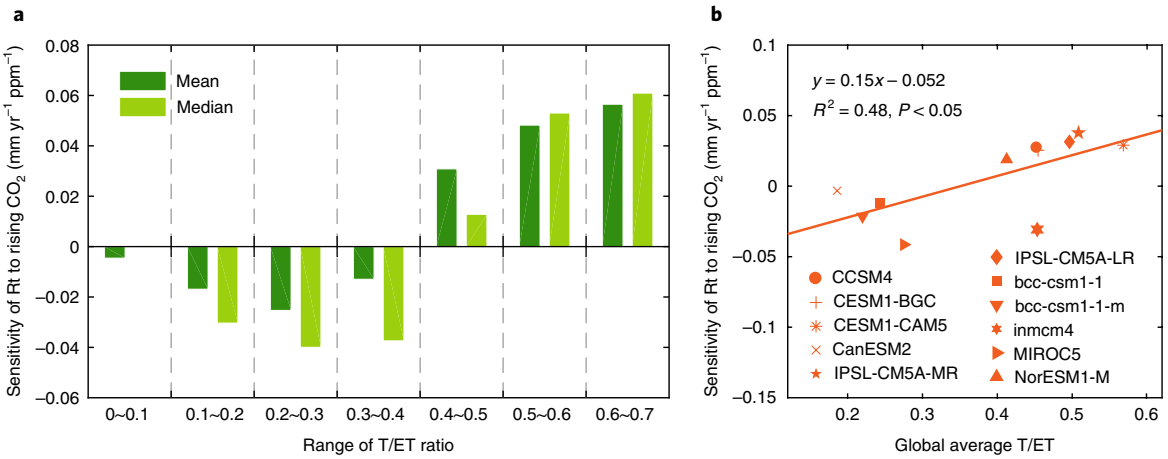

Fig. 5 Impact of modelled T/ET on the runoff responses to rising atmospheric CO_2. a, The average and median of the sensitivity of runoff (Rt), via transpiration process response, to atmospheric CO_2 concentration as a function of T/ET levels binned into 0.1 intervals. Rt represents the difference between runoff and rainfall to exclude the effects of CO_2-induced rainfall changes. Both Rt and T/ET values are from different geographical points of the CMIP5 ensemble mean results (from the 1pctCO2 simulation). **b**, Scatterplot of the modelled sensitivity of the global average Rt to atmospheric CO_2 concentration versus the modelled global average T/ET ratios.

FLUXNET observations ($1.23 \pm 0.03\,gC\,m^{-2}\,MJ^{-1}$ APAR)[33]. This negatively biased LUE leads to an underestimation in the ecosystem photosynthetic rate, and consequently in canopy transpiration. Accordingly, we obtained a higher ensemble mean global T/ET of 0.52 ± 0.11 through incorporating the observation-based LUE value into the CMIP5 results (Supplementary Text 5).

Alongside potential errors in photosynthetic response, other biases in T/ET could also occur through deficiencies in the rooting characteristics (depth, thickness and density), vertical soil properties (soil texture, hydraulic conductivity and moisture gradients), stomatal conductance (for example, response to atmospheric moisture demand) and canopy interception processes[3,10,34,35]. A rooting depth of no more than 2–4 m is widely adopted by most land surface models[36], yet this will underestimate the capacity for deep-rooted vegetation over a wide range of biomes[37,38] to access water and thus transpire. Newly published root water-uptake depth data[38] report plant roots to be substantially deeper than 4 m over deciduous and evergreen broadleaf forests. In addition, shrubs are currently ignored by most ESMs in spite of their high ability to transpire more water due to their deeper roots[39]. Furthermore, the contribution of the understorey vegetation to transpiration in forests is not taken into account in most ESMs, which may also suppress the ESM-estimated T/ET. Finally, the parameterization of canopy interception processes remains simple in the ESMs, which is, in most cases, formulated as a function of vegetation density and rainfall volume[40]. However, canopy interception observations reported this component of ET to be sensitive also to vegetation type and structure, and to rain characteristics, which include intensity and frequency[35].

To test whether the simulation of interception loss affects the global T/ET ratio, we plot this ratio against corresponding global interception loss estimates across all the ESMs (Supplementary Fig. 7a). We find that the modelled interception loss explains 22% of the cross-model variance of global T/ET. Models with higher global T/ET ratios simulate less interception loss, and hence leave more water available for transpiration. Compared with satellite-based global interception estimates[41], the modelled global interception loss is subject to a strong positive bias ($141 \pm 43\,mm\,yr^{-1}$ of the model ensemble mean versus $62 \pm 12\,mm\,yr^{-1}$ (Supplementary Fig. 7)). We verify that this overestimate is not due to PRE inputs in the ESMs being too high by showing a similar result with the modelled interception loss normalized by the PRE amount (Supplementary Fig. 7b). Hence, we provide direct evidence that the simplistic treatment of canopy interception loss and re-evaporation processes results in an excess ET partitioning into interception in CMIP5 models. This error partially contributes to our identified too low T/ET values in the ESMs. This highlights the necessity for more accurate representations of canopy interception processes in the ESMs, which include the impact of rainfall intensity and subgrid rainfall variability on interception loss[42].

Implications of improved T/ET modelling

Plant transpiration depends on vegetation physiological characteristics[43] and is expected to evolve in response to rising atmospheric CO_2 and climate change. Hence, the strong underestimation in the T/ET ratio of some models brings uncertainty to the simulated future terrestrial water cycle and surface energy balances. For example, Zeng et al.[6] demonstrated that extremely low T/ET levels in two climate models led to an underestimated sensitivity of the modelled ET to the known increases of LAI ('greening'). This causes an underestimated cooling in the surface temperature contributed by the Earth's greening. Analogously, the general underestimation of T/ET in the ESMs, as examined here, implies an overall underestimation in the strength of vegetation biophysical cooling effects[5,6], for both the present and future climatic states. Higher T/ET levels have the potential to attenuate surface warming, and therefore dampen the magnitude and frequency of droughts and heatwaves under climate change. This is relevant because the likelihood of weather extremes increases as temperature goes up[44], so more accurate projections of T/ET will help characterize this natural mitigation.

T/ET levels also modulate the extent to which terrestrial runoff is affected by rising atmospheric CO_2 through stomata closure and leaf area changes. Using the CMIP5 1pctCO2 simulation with an idealized 1% yr^{-1} increase in atmospheric CO_2 concentration up to quadrupling the preindustrial CO_2 concentration, we investigate geographical differences in runoff changes compared to their simulated T/ET levels, and the cross-model relationship between the magnitude of global-mean runoff changes and T/ET levels. Specifically, we record the modelled runoff changes through the transpiration process response, $\Delta Rt(\Delta CO_2, T/ET)$, as a function of CO_2 and the local T/ET value, after subtracting the effects of CO_2-induced changes in precipitation, ΔPRE (that is, $\Delta Rt = \Delta Runoff - \Delta PRE$). Mean and median values of $\partial Rt/\partial CO_2$ are presented in Fig. 5a, based on binned T/ET values from the geographical variation of the ESM ensemble mean result. We find that regions with

higher T/ET values have a larger and positive Rt increase as CO_2 increases ($P<0.05$). Of particular interest is that for low T/ET values (T/ET < 0.2, generally over regions with limited vegetation cover, and thus a weak stomatal response) a negative runoff response to rising CO_2 is detected (Fig. 5a). This is caused by leaf area increases (greening raising T) dominating stomata closure (lowering T), thus creating a net transpiration increase. This effect of CO_2-induced changes of T/ET on runoff is also corroborated by looking at the ESMs individually. We find that ESMs with broadly higher global-mean T/ET ratios (rather than considering gridbox binned values) also simulate higher Rt increase responding to rising atmospheric CO_2 (Fig. 5b). Hence, where terrestrial water is more intensely recycled by transpiration, there is also a stronger suppression of transpiration as CO_2 increases and thus more rainfall enters the streams and rivers.

As a biological pump of water from the land surface to the atmosphere, vegetation plays an important role in regulating water and energy exchange between the land surface and the atmosphere[1,5,6]. To understand this role of vegetation is vital for climate mitigation and water resource management in future climate conditions, especially as physiological processes are responsive to changed local meteorological conditions under global warming and rising atmospheric CO_2 concentration[43,45]. Changing transpiration levels will impact freshwater availability, knowledge of which is a key prerequisite for policy development in an evolving climate. Furthermore, different land–atmosphere exchanges of water could influence future atmospheric humidity levels, and as water is itself a greenhouse gas, this could modulate warming rates[46]. Even for present-day climatic conditions, measurements show unequivocally that transpiration comprises the largest fraction of global land ET. However, this fundamental role of terrestrial vegetation is currently poorly modelled; our emergent constraint approach demonstrates that CMIP5 ESMs broadly underestimate T/ET. The additional novel evaluation framework applied here confirms that leaf area is the dominant driver of modelled T/ET variability, as reported by observation-based studies[10,24]. Yet we find it is not inaccurate leaf cover values that directly cause the T/ET values to be too low, but instead the parameterization of how vegetation functions for different LAI values. Hence, further efforts are required to address the currently underrepresented processes in the ESMs, for instance, by routinely incorporating a radiative transfer scheme that accounts for the effect of diffuse sunlight, reassessing the precise ecosystem photosynthetic rate that relates to transpiration, modelling deeper rooting systems as guided by the available plant rooting-depth data[38] and providing more realistic parameterization of canopy hydrological processes, which include interception loss.

References

1. Jasechko, S. et al. Terrestrial water fluxes dominated by transpiration. *Nature* **496**, 347–350 (2013).
2. Jung, M. et al. Recent decline in the global land evapotranspiration trend due to limited moisture supply. *Nature* **467**, 951–954 (2010).
3. Wang, K. & Dickinson, R. E. A review of global terrestrial evapotranspiration: observation, modeling, climatology, and climatic variability. *Rev. Geophys.* **50**, RG2005 (2012).
4. Zhang, Y. et al. Multi-decadal trends in global terrestrial evapotranspiration and its components. *Sci. Rep.* **6**, 19124 (2016).
5. Alkama, R. & Cescatti, A. Biophysical climate impacts of recent changes in global forest cover. *Science* **351**, 600–604 (2016).
6. Zeng, Z. et al. Climate mitigation from vegetation biophysical feedbacks during the past three decades. *Nat. Clim. Change* **7**, 432–436 (2017).
7. Schlesinger, W. H. & Jasechko, S. Transpiration in the global water cycle. *Agric. For. Meteorol.* **189–190**, 115–117 (2014).
8. Good, S. P., Noone, D. & Bowen, G. Hydrologic connectivity constrains partitioning of global terrestrial water fluxes. *Science* **349**, 175–177 (2015).
9. Martens, B. et al. GLEAM v3: satellite-based land evaporation and root-zone soil moisture. *Geosci. Model Dev. Discuss.* **10**, 1903–1925 (2017).
10. Wei, Z. et al. Revisiting the contribution of transpiration to global terrestrial evapotranspiration. *Geophys. Res. Lett.* **44**, 2792–2801 (2017).
11. Sutanto, S. et al. HESS opinions: a perspective on different approaches to determine the contribution of transpiration to the surface moisture fluxes. *Hydrol. Earth Syst. Sci.* **11**, 2583–2612 (2014).
12. Kool, D. et al. A review of approaches for evapotranspiration partitioning. *Agric. For. Meteorol.* **184**, 56–70 (2014).
13. Coenders-Gerrits, A. M. et al. Uncertainties in transpiration estimates. *Nature* **506**, E1–2 (2014).
14. Schlaepfer, D. R. et al. Terrestrial water fluxes dominated by transpiration: comment. *Ecosphere* **5**, 1–9 (2014).
15. Maxwell, R. M. & Condon, L. E. Connections between groundwater flow and transpiration partitioning. *Science* **353**, 377–380 (2016).
16. Evaristo, J., Jasechko, S. & McDonnell, J. J. Global separation of plant transpiration from groundwater and streamflow. *Nature* **525**, 91–94 (2015).
17. Milly, P. C., Dunne, K. A. & Vecchia, A. V. Global pattern of trends in streamflow and water availability in a changing climate. *Nature* **438**, 347–350 (2005).
18. Seager, R. et al. Projections of declining surface-water availability for the southwestern United States. *Nat. Clim. Change* **3**, 482–486 (2012).
19. Taylor, R. G. et al. Ground water and climate change. *Nat. Clim. Change* **3**, 322–329 (2012).
20. Taylor, K. E., Stouffer, R. J. & Meehl, G. A. An overview of CMIP5 and the experiment design. *Bull. Am. Meteorol. Soc.* **93**, 485–498 (2012).
21. Cox, P. M. et al. Sensitivity of tropical carbon to climate change constrained by carbon dioxide variability. *Nature* **494**, 341–344 (2013).
22. Mystakidis, S., Davin, E. L., Gruber, N. & Seneviratne, S. I. Constraining future terrestrial carbon cycle projections using observation-based water and carbon flux estimates. *Glob. Change Biol.* **22**, 2198–2215 (2016).
23. Wenzel, S., Cox, P. M., Eyring, V. & Friedlingstein, P. Projected land photosynthesis constrained by changes in the seasonal cycle of atmospheric CO_2. *Nature* **538**, 499–501 (2016).
24. Villegas, J. C. et al. Sensitivity of regional evapotranspiration partitioning to variation in woody plant cover: insights from experimental dryland tree mosaics. *Glob. Ecol. Biogeogr.* **24**, 1040–1048 (2015).
25. Lloyd, J. et al. Optimisation of photosynthetic carbon gain and within-canopy gradients of associated foliar traits for Amazon forest trees. *Biogeosciences* **7**, 1833–1859 (2010).
26. Clark, D. et al. The Joint UK Land Environment Simulator (JULES), model description—Part 2: carbon fluxes and vegetation dynamics. *Geosci. Model Dev.* **4**, 701–722 (2011).
27. Gu, L. et al. Response of a deciduous forest to the Mount Pinatubo eruption: enhanced photosynthesis. *Science* **299**, 2035–2038 (2003).
28. Mercado, L. M. et al. Impacts of changes in diffuse radiation on the global land carbon sink. *Nature* **458**, 1014–1017 (2009).
29. Knohl, A. & Baldocchi, D. D. Effects of diffuse radiation on canopy gas exchange processes in a forest ecosystem. *J. Geophys. Res. Biogeosci.* **113**, G02023 (2008).
30. Oliveira, P. J. C., Davin, E. L., Levis, S. & Seneviratne, S. I. Vegetation-mediated impacts of trends in global radiation on land hydrology: a global sensitivity study. *Glob. Change Biol.* **17**, 3453–3467 (2011).
31. Berry, J. A., Beerling, D. J. & Franks, P. J. Stomata: key players in the earth system, past and present. *Curr. Opin. Plant Boil.* **13**, 232–239 (2010).
32. Keenan, T. F. et al. Increase in forest water-use efficiency as atmospheric carbon dioxide concentrations rise. *Nature* **499**, 324–327 (2013).
33. Wei, S., Yi, C., Fang, W. & Hendrey, G. A global study of GPP focusing on light-use efficiency in a random forest regression model. *Ecosphere* **8**, e01724. (2017).
34. Lawrence, D. M., Thornton, P. E., Oleson, K. W. & Bonan, G. B. The partitioning of evapotranspiration into transpiration, soil evaporation, and canopy evaporation in a GCM: impacts on land–atmosphere interaction. *J. Hydrometeorol.* **8**, 862–880 (2007).
35. Llorens, P. & Domingo, F. Rainfall partitioning by vegetation under Mediterranean conditions. A review of studies in Europe. *J. Hydrol.* **335**, 37–54 (2007).
36. Heitman, J., Horton, R., Sauer, T. & DeSutter, T. Sensible heat observations reveal soil-water evaporation dynamics. *J. Hydrometeorol.* **9**, 165–171 (2008).
37. Yang, Y., Donohue, R. J. & McVicar, T. R. Global estimation of effective plant rooting depth: implications for hydrological modeling. *Wat. Resour. Res.* **52**, 8260–8276 (2016).

38. Fan, Y., Miguez-Macho, G., Jobbágy, E. G., Jackson, R. B. & Otero-Casal, C. Hydrologic regulation of plant rooting depth. *Proc. Natl Acad. Sci. USA* **114**, 10572–10577 (2017).
39. Parolari, A. J., Goulden, M. L. & Bras, R. L. Ecohydrological controls on grass and shrub above-ground net primary productivity in a seasonally dry climate. *Ecohydrology* **8**, 1572–1583 (2015).
40. Oleson, K. W. et al. Technical description of version 4.0 of the Community Land Model (CLM). *Geophys. Res. Lett.* **37**, 256–265 (2010).
41. Miralles, D. G., Gash, J. H., Holmes, T. R. H., de Jeu, R. A. M. & Dolman, A. J. Global canopy interception from satellite observations. *J. Geophys. Res.* **115**, D16122 (2010).
42. Wang, D., Wang, G. & Anagnostou, E. N. Impact of sub-grid variability of precipitation and canopy water storage on hydrological processes in a coupled land–atmosphere model. *Clim. Dynam.* **32**, 649–662 (2009).
43. Field, C., Jackson, R. & Mooney, H. Stomatal responses to increased CO_2: implications from the plant to the global scale. *Plant Cell Environ.* **18**, 1214–1255 (1995).
44. Fischer, E. M. & Knutti, R. Anthropogenic contribution to global occurrence of heavy-precipitation and high-temperature extremes. *Nat. Clim. Change* **5**, 560–564 (2015).
45. Swann, A. L., Hoffman, F. M., Koven, C. D. & Randerson, J. T. Plant responses to increasing CO_2 reduce estimates of climate impacts on drought severity. *Proc. Natl Acad. Sci. USA* **113**, 10019–10024 (2016).
46. Solomon, S. et al. Contributions of stratospheric water vapor to decadal changes in the rate of global warming. *Science* **327**, 1219–1223 (2010).

Acknowledgements

This study was supported by the National Natural Science Foundation of China (41561134016 and 41530528), the 111 Project (B14001) and the National Youth Top-notch Talent Support Program in China. C.H. is grateful for funding from the Centre for Ecology and Hydrology National Capability fund in the UK.

Author contributions

S.P. designed the research; X.L. performed the analysis; X.L., S.P. and C.H. drafted the paper and all the authors contributed to the interpretation of the results and to the text.

Competing interests

The authors declare no competing interests.

Methods

CMIP5 outputs. The historical (analysed years 1980–2005) and Representative Concentration Pathway 8.5 (ref. [20]) scenario (analysed years 2080–2100) simulations of monthly ET, transpiration and relevant driving environmental factors (Supplementary Table 3) were obtained from the CMIP5 archive[20] (http://cmip-pcmdi.llnl.gov/cmip5/). A total of 19 ESMs were available for the study period 1980–2005, which provide all the diagnostic variables that are required for this study. Of these ESMs, 16 also had available required outputs for the corresponding future projections during 2080–2100 (Supplementary Table 1). All the CMIP5 outputs were linearly interpolated from their native resolution to a common 1°×1° global grid. If any model had more than one ensemble member (that is, starting with different initial conditions), then an average was taken over all the monthly realizations. The monthly vapour pressure deficit was calculated as the difference between the modelled saturation and the actual vapour pressure using monthly temperature, surface pressure and relative humidity[47]. The 10 m wind speed (WS) from most climate models was calculated using 10 m north- and eastward wind speed, except the five models without direct outputs of 10 m wind fields (that is, CCSM4, CESM1-BGC, CESM1-CAM5, CESM1-FASTCHEM and CESM1-WACCM). For these five models, WS was extrapolated from the wind speed at the closest pressure level based on a power-law velocity profile equation[48,49]. Our study region is restricted to the global vegetation covered land surface, defined as where multiyear average satellite observed LAI > 0.1.

Observational data. Field observations of T/ET across 35 sites (listed in Supplementary Table 2) were compiled from 33 individual publications (by January 2017) that experimentally measured at least three out of the four relevant variables, that is, ET, soil evaporation, transpiration and interception loss. We only retained site observations that were complete for at least an annual period and at least at a monthly time step. These site observations were measured via a range of approaches, including stable isotopes, microlysimeters, chamber experiments or a combination of sap flow and eddy covariance (Supplementary Table 2). Two observational sites were located on small islands (Vanuatu and Hawaii) that were not represented in the ESMs due to spatial resolution limitations, so they were excluded in this analysis. Uncertainty bounds of the T/ET observations at nine sites were not available (Supplementary Table 2), so their s.d. value was assumed to be the average of the s.d. values available at other sites (that is, 7.4%). The site-average T/ET value across the 33 sites and its uncertainty bound provide the single value with a range, which was used in the emergent constraint on the global magnitude of T/ET (horizontal axis in Fig. 2a).

To investigate whether the underestimated T/ET values in the ESMs are derived from the modelled biases of dominant driving variables, including LAI, temperature (TMX or DTR), water availability (SWC or PRE) and RN, we obtained measurements of these variables independently from satellite and/or ground-based observations and reanalysis data sets. We employed LAI observations from the Global Inventory Modeling and Mapping Studies (GIMMS) LAI3g data set, which is produced from the third-generation AVHRR GIMMS NDVI data set using an artificial neural network model[50]. The LAI observation has gone through strict quality validation through comparisons with field measurements and satellite-observed products. It covers the period from July 1981 to December 2014 and is available at 1/12° spatial resolution and 15 day temporal resolution. Remote sensing radiative flux data, which include shortwave and longwave solar radiation (both up- and downwelling fluxes that were combined to give RN), were derived from the NASA World Climate Research Programme/Global Energy and Water-Cycle Experiment Surface Radiation Budget (SRB Release 3.0) (http://gewex-srb.larc.nasa.gov/). These radiation observations were provided at a spatial resolution of 1°×1° and a monthly temporal resolution that spanned from July 1983 to December 2007. Other meteorological variables (that is, the maximum/minimum near surface 2 m air temperature and PRE) came from Climate Research Unit TS3.22 (http://www.cru.uea.ac.uk/data/)[51] that covers the full 1980–2005 period. The total soil moisture content from the ERA-Interim reanalysis output was used in this study as a surrogate for soil moisture observations due to the lack of direct global-coverage soil moisture maps. All these environmental variables were first linearly re-gridded to the common 1°×1° global grid and then averaged over the study period 1980–2005.

Emergent constraint method. ESMs often exhibit significant differences between them, and for a variety of aspects of the climate system. This can make it difficult to understand fully the contemporary climate or to estimate future changes. However, recently the method of 'emergent constraints' was developed and utilised to reduce the uncertainty that surrounded multiple features of the Earth system. The basic concept is that, although ESMs do differ, there are across them various robust one-to-one relationships (emergent constraints) that emerge when the multimodel outputs are analysed. These relationships often link pairs of model-derived quantities of interest. The first one is usually a quantity of key importance that describes how the Earth system operates, but for which the true value is unknown, whereas the second diagnostic might be a quantity for which measurements are available. From this, it is possible to use measurements of the second variable, via the emergent constraint, to constrain the first quantity. For example, based on a model-derived relationship between the long-term sensitivity of carbon to warming and the short-term responses of atmospheric CO_2 to warming, Cox et al.[21] utilised contemporary observations to constrain the sensitivity of tropical carbon storage to climate change.

The rationale for our emergent constraint on global T/ET comes from the strong heuristic linear relationship between global-averaged T/ET and site-averaged T/ET across the CMIP5 ESMs (Fig. 2a). Similar to the constraining approach performed by Cox et al.[21], we utilised this model-based relationship with 33 field measurements of T/ET, which, via this emergent constraint, imposed much smaller uncertainty bounds on the global T/ET estimates compared to the spread of ESM-based global T/ET values. The conditional probability density function (PDF) for the constrained global T/ET (green dashed line in Fig. 2b) was derived[21] from the prior PDF of site observations, together with the model-based linear relationship (Fig. 2a).

To test the robustness of our constrained result of the global T/ET, a number of additional sensitivity analyses were performed. Although the observational periods (lasting at least 1 yr) of the available sites differ between locations, and are much shorter than the averaging periods of the model results (1980–2005), this causes negligible impact on our global constrained value. This is due to the weak interannual variability of ESM-modelled T/ET values for all site locations (s.d. of T/ET values ≤0.02). In addition, the constrained result is not sensitive to the number of sites included, as verified by randomly and repeatedly selecting a subset of site measurements to derive global T/ET estimates (Supplementary Text 1). Almost all combinations of over ten sites could lead to an estimate close to that obtained from all 33 sites, with a stochastic error of <0.05 in global T/ET (Supplementary Fig. 1). We also derived a very similar result (0.64 ± 0.05 (Supplementary Fig. 3)) if we excluded those sites where the known local vegetation type is not representative of the dominant vegetation type of the corresponding ESM grid cells (Supplementary Text 1 and Supplementary Table 2). In a final test, we confirmed that the use of coarse ESM pixels to represent the site-level signal had a weak impact on the constrained value (0.67 ± 0.07 (Supplementary Fig. 2)). We achieved this by performing the same analysis, but using modelled 'climate analogue' ESM grid cells in which the climatic conditions are nearest to the site-level climatology (Supplementary Text 1). All of these additional tests confirm a systematic underestimation in the ESM-modelled T/ET values, based on our emergent constraint approach that entrains site-level local measurements of T/ET.

BRTs. BRT is a powerful machine-learning approach based on traditional regression tree methods[52,53]. It was employed here to investigate the environmental drivers that determine the spatial variations of T/ET in each ESM. This BRT analysis was performed using the 'dismo' and 'gbm' packages in the R statistical software, and details of the procedures used to establish the BRT models are described in Supplementary Text 2. Using BRTs built with CMIP5 outputs, the relative importance of environmental variables, as well as the partial dependency of T/ET on each variable, were quantified. For each of the 19 ESMs, the dominant drivers were defined as those that explained over 10% of the spatial variations in T/ET, being either LAI, temperature (TMX or DTR), water availability (SWC or PRE) or RN. The 19 CMIP5 models could be categorized into five groups with different combinations of dominant drivers: (1) dominated by only LAI (CCSM4, CESM1-BGC, CESM1-CAM5, CESM1-FASTCHEM, CanESM2, MIROC-ESM, MIROC-ESM-CHEM, MIROC4h, MIROC5, NorESM1-M and inmcm4), (2) dominated by LAI and temperature (GFDL-ESM2G and GFDL-ESM2M), (3) dominated by LAI and water availability (IPSL-CM5A-LR, IPSL-CM5A-MR and bcc-csm1-1-m), (4) dominated by LAI, temperature and water availability (MRI-ESM1 and bcc-csm1-1) and (5) dominated by LAI, temperature and radiation (CESM1-WACCM).

The BRT algorithm allows the replacement of the dominant CMIP5-based drivers that govern the spatial variations of T/ET with corresponding observations, and thus creates new global estimates of T/ET. This enables the uncoupling of potential errors in the T/ET projections due to incorrect surface projections of the drivers from any deficiencies in the land surface components of the ESMs. Using the BRT method as a tool to partition the role of the dominant drivers, five sequential sets of new simulations were performed with observation-based gridded fields replacing model-based fields, as follows: (1) LAI only, (2) LAI and temperature (DTR and TMX), (3) LAI and water availability (SWC and PRE), (4) LAI and RN, and (5) all variables (LAI, DTR, TMX, SWC, PRE and RN). To eliminate the influence from potential interactions between LAI and other environmental factors, the biases in global T/ET that stemmed from temperature, water availability and radiation were calculated as the difference between simulation (1) and simulations (2), (3) and (4), respectively.

Data availability. Supplementary Information lists the site-based T/ET measurements analysed in this study. The CMIP5 model outputs are available from the CMIP5 archive (http://cmip-pcmdi.llnl.gov/cmip5/).

References

47. Zhao, M. & Running, S. W. Drought-induced reduction in global terrestrial net primary production from 2000 through 2009. *Science* **329**, 940–943 (2010).

48. Archer, C. L. & Jacobson, M. Z. Spatial and temporal distributions of U.S. winds and wind power at 80 m derived from measurements. *J. Geophys. Res. Atmos.* **108**, 469–474 (2003).
49. Devis, A., Demuzere, M. & van Lipzig, N. P. M. A height dependent evaluation of wind and temperature over Europe in the CMIP5 Earth System Models. *Clim. Res.* **61**, 41–56 (2014).
50. Zhu, Z. et al. Global data sets of vegetation leaf area index (LAI)3g and fraction of photosynthetically active radiation (FPAR)3g derived from Global Inventory Modeling and Mapping Studies (GIMMS) Normalized Difference Vegetation Index (NDVI3g) for the period 1981 to 2011. *Remote Sens.* **5**, 927–948 (2013).
51. Harris, I., Jones, P. D., Osborn, T. J. & Lister, D. H. Updated high-resolution grids of monthly climatic observations—the CRU TS3.10 Dataset. *Int. J. Climatol.* **34**, 623–642 (2014).
52. De'ath, G. Boosted trees for ecological modeling and prediction. *Ecology* **88**, 243–251 (2007).
53. Elith, J., Leathwick, J. R. & Hastie, T. A working guide to boosted regression trees. *J. Anim. Ecol.* **77**, 802–813 (2008).

Supplementary Information

Text S1. Test on the robustness of the "emergent constraint" approach

To verify the robustness of our emergent constraint results, several additional checks were performed. First, we investigated the sensitivity of the calculated constrained global T/ET to the number of site measurements used. We derived an ensemble of global T/ET estimates using a subset (ranging from 1 to the full amount of available sites, i.e., 33) of site observations. Specifically, for each number κ ($1 \leq \kappa \leq 33$), we re-calculated the global T/ET using κ sites randomly selected from the full set of available sites, and repeated this procedure 100 times to examine uncertainties from this stochastic site selection. Second, we recognized that in situ measurements may not be representative of ESM-modelled T/ET and meteorological drivers within a related $1° \times 1°$ grid cell area. As a result, we also performed the same "emergent constraint" but to climatically analogue model grid-cells, rather than to the exact location-specified model grid-cells. Specifically, 'climate analogue' grid-cells refer to where the local climatic model conditions are similar to that measured at each experimental site, i.e., areas with temperature, precipitation and radiation within $\pm 15\%$ of the magnitude of site-level climatology (Supplementary Table 2). Where values of these quantities are not available at the sites, we took these directly from the WorldClim[54] climatic dataset at 1-km resolution and based on meteorological station data during 1970-2000. Two observational sites were excluded from this analysis since there is no 'climate analogue' pixels available for all ESMs. In addition, similar analysis was performed excluding measurement sites where observed vegetation type does not represent the dominant vegetation type of the corresponding grid-cells (Supplementary Fig. 3). Different land cover maps are adopted in

ESMs to describe plant functional type (PFT) fractions across the ESMs, and in some instances, there is a lack of detailed information on vegetation distribution in ESMs, hence we instead used the Moderate-resolution Imaging Spectroradiometer (MODIS) land cover maps (MCD12C1) with a 1-km resolution for the period 2001-2005. MODIS land cover maps were first aggregated into a 1°×1° global grid to calculate the fraction of each land cover type in grid cells of that size. From this, we defined the dominant vegetation type of the corresponding pixels at each observational sites.

Text S2. Boosted regression trees (BRT)

All land surface models in ESMs solve numerically sets of differential equations, which are available for analysis from each modelling centre. However, across a very large number of climate models such as in the CMIP5 ensemble, it is more practical to reconstruct ecosystem model response via statistical techniques. BRT, as used in this study, is an advanced regression (machine learning) technique to link driving forcings to a target variable requiring prediction. It is a stochastic extension of traditional regression trees, but "boosted" by integrating additional, sequential "trees" that model the residuals in randomized subsets of the data[52,53]. Due to its strong predictive capability, easy interpretability[55] and capacity to deal with complex nonlinearities, this method has been increasingly advocated for ecological analyses[52], and is thus a suitable tool for our analysis. Each climate model provides a large number of diagnostics in space and time, hence the BRT approach is very accurate in reconstructing dominant responses. Here we apply the BRTs to ESM outputs, to examine which and how environmental drivers govern the global variation of T/ET in each ESM.

As with most machine learning techniques, it was first necessary to train with available data, and here as the spatial variations of T/ET (i.e., response variable) and the 14 key environmental factors (i.e., predictor variables, listed in Supplementary Table 3) averaged over the 1982–2005 period. This was done using global set of land grid cells in each ESM. All BRT runs shared a common suite of metaparameters, including gaussian error distribution, a learning rate of 0.01, an interaction depth of 5, and a bag fraction of 0.5 (full details of these method parameters and implications in ref. 52). This approach then identifies the optimal number of "trees" for each ESM via a stepwise procedure that incorporated a fixed number of trees into the tree ensemble until realizing a minimum predictive error[53]. The goodness-of-fit of each run was determined by evaluating the fitted model against a group of independent data (20% of the total grid samples) using ten-fold cross-validation approach[52,53]. The final step of establishing BRT framework is to determine any "nuisance parameters". Our BRT models with all predictors was pruned through progressively eliminating the least-informative variable until average reduction in predictive deviance exceeds its original standard error[53]. After refitting with these statistically important variables retained in the last procedure, BRTs were used to determine first the relative contributions of environmental variables to the spatial variation of T/ET, and second the partial dependency (defined as the marginal effect of a variable on the response when all other variables are held at their average) of T/ET on these driving quantities.

Text S3. Implications for modeled T/ET by correcting the dominant drivers

Beside LAI, we also test whether any bias in each of the other dominant drivers (i.e., drivers related to temperature, water availability and solar radiation) results in the underestimation in global T/ET. For temperature-related variables (daily maximum temperature, TMX; and diurnal temperature range, DTR), the two IPSL models (i.e., IPSL-CM5A-M and IPSL-CM5A-LR) produce a considerable positive bias in temperature (DTR > 8K and TMX > 3K) compared with observation (Supplementary Fig. 5a); global T/ET in IPSL models further decreases by 27% with this temperature-related bias corrected (Supplementary Fig. 5b). Variables related to water availability (soil water content, SWC; and precipitation, PRE) simulated by CMIP5 models also show strong biases against ERA-Interim reanalysis data set (as an alternative to soil moisture observations, which are generally unavailable) and precipitation from Climate Research Unit (CRU) data set (Supplementary Fig. 5a). Twelve ESMs largely overestimated the total SWC (> 50%) compared to reanalysis output, and the majority (17 in 19) of ESMs slightly overestimated PRE (6 – 24%) compared to CRU data. When observed SWC and PRE are accounted for, via the BRT algorithm, this once again causes a general decrease in global T/ET, in particular for the IPSL and GFDL models (Supplementary Fig. 5c). Since net radiation (RN) produced by the CMIP5 models is generally consistent with satellite observation, replacing RN does not change global T/ET significantly (paired-samples *t* test, P = 0.16) (Supplementary Fig. 5a, d).

Text S4. An adjusted big-leaf model for T/ET

The land surface component of most ESMs does not calculate explicit variation of in-canopy light levels. Instead, they utilize a light extinction coefficient (τ) to estimate surface energy

exchanges, which in turn influences terrestrial carbon assimilation fluxes. To assess the effect of any bias in global T/ET associated through inaccurate representation of τ (for discussion of errors in standard values of τ, see ref. 25), an adjusted big-leaf model is developed to approximate the carbon sequestration and transpiration processes for each ESM. This approximation is based on the partial dependence of ESM-modeled T/ET against LAI (Fig. 4b) and an exponential extinction of light in the canopy relating to LAI. Only ESMs providing direct gross primary production (GPP) outputs are taken into consideration in this analysis, as simultaneous use of both carbon and water fluxes are needed as follows to identify τ.

The big-leaf assumption[26,56] is that leaf photosynthesis rate is assumed to decay exponentially with the vertical gradient of cumulative leaf area. Accordingly, canopy-level photosynthesis rate (A_c, $\mu mol\ m^{-2}\ s^{-1}$) is the accumulated leaf-level photosynthesis rate across the entire canopy leaf area, and is given as:

$$A_c = \int_0^{LAI} A_0 e^{-\tau L} dL = A_0 \frac{\left(1 - e^{-\tau LAI}\right)}{\tau} \quad (1)$$

Here τ is the light extinction coefficient, A_0 is the leaf photosynthesis rate at the top of canopy ($\mu mol\ m^{-2}\ s^{-1}$), and L is the cumulative leaf area index measured downwards from the canopy top ($L = 0$ for the uppermost leaves of the canopy and $L =$ LAI for the total canopy leaf area index). Although A_0 in models may vary spatially and temporally, its exact value cannot be reproduced outside the model simulations. This is because A_0 depends on multiple drivers absent in ESM outputs, such as the type of photosynthetic pathway (C_3 or C_4), leaf nitrogen concentration and the incident photosynthetically active radiation[26].

Therefore, in the derivation of τ, we assumed this variable to be an ESM-specific constant, representing the spatial and time average of carbon sequestration capacity A_0, thus giving a general mean value across all driving forcings and limitations (e.g., nutrient availability and drought).

By linking water loss to carbon assimilation through stomata behaviors, transpiration flux was then scaled up to be canopy level using the following formula:

$$\frac{T}{ET} = \frac{A_c}{WUE \cdot ET} = \frac{A_0}{WUE \cdot ET} \cdot \frac{\left(1 - e^{-\tau LAI}\right)}{\tau} \quad (2)$$

Here WUE is the plant water use efficiency defined as the ratio of CO_2 assimilated to transpired H_2O during the photosynthesis, and is a direct diagnostic from ESMs of GPP/T. A nonlinear curve-fitting algorithm (using the "lsqcurvefit" function in MATLAB; http://www.mathworks.co.uk/products/matlab/) was adopted for each ESM to optimize the implicit extinction coefficient τ and maximum top-canopy carbon assimilation rate A_0, by minimizing the least squares error for the modeled local T/ET values. This approximation is based on the partial dependence of T/ET against LAI shown in Fig. 3b, and also partial dependences of WUE and ET on LAI derived from the BRT simulations (not shown).

The big-leaf based modelling structure then enables our final step to be made of explaining how overestimation of τ could cause major underestimation of T/ET. Specifically, we take our big-leaf model and best-fit solvers for A_0 and τ (Supplementary Table 4), but then instead consider lower τ values ($0.2 \leq \tau \leq$ the fitting value, based on available field observations of τ provided by ref. 25), whilst keeping LAI values held at the

ESM-simulated global average, and adopting WUE and ET values corresponding to the LAI constants based on ESM-derived partial dependency. New values of T/ET are then derived from Equation S2.

Text S5. Evaluation on modeled light-use efficiency

In addition to the characterization of τ, global rate of photosynthesis (and thus transpirational rate) is also largely determined by the maximum carbon assimilation rate A_0. As a good indicator for the photosynthetic capacity A_0, light use efficiency (LUE) from ESMs is here evaluated against a data-driven LUE product[33]. For each ESM, we first converted incoming shortwave solar radiation into photosynthetically active radiation (PAR), using a constant ratio of 0.48 MJ (PAR) MJ^{-1} (radiation)[57]. Since ESMs do not explicitly calculate the total fraction of incident PAR absorbed by plant canopies (FPAR), we indirectly derived it from modeled LAI via the Beer-Lambert approximation:

$$FPAR = 0.95\left(1-\exp\left(-\tau \cdot LAI\right)\right) \tag{3}$$

where τ is the light extinction coefficient calculated by the adjusted "big-leaf" model (see Supplementary Text 4). Then ESM-simulated LUE was indirectly obtained as

$$LUE = \frac{GPP}{APAR} = \frac{GPP}{FPAR \cdot PAR} \tag{4}$$

A newly published paper[33] released a data-driven LUE product, which is obtained by upscaling FLUXNET LUE estimates using a random forest regression approach. Ecosystem types, as widely suggested to be important in determining LUE (e.g., ref. 58), was incorporated to represent climate/meteorological information in the machine-learning modeling. The quality of this dataset was not directly assessed due to the lack of large-scale

LUE observations, but good performance could be expected from the validation of the LUE-derived GPP estimates (GPP=PAR×FPAR×LUE) against FLUXNET-based diagnostic GPP data[33]. At the global scale, average LUE was reported to be 1.23 ± 0.03 $g\ \mathrm{C}\ m^{-2}\ MJ^{-1}APAR$ during 2001-2005, which is here considered as a benchmark for ESM results. Finally, we re-calculated the modeled transpiration rate (and thus global T/ET), by combining ESM results with this observation-based LUE value (LUE_{obs}):

$$T = \frac{GPP}{WUE} = \frac{PAR \times FPAR \times LUE_{obs}}{WUE} \tag{4}$$

References

54. Hijmans, R. J., Cameron, S. E., Parra, J. L., Jones, P. G. & Jarvis, A. Very high resolution interpolated climate surfaces for global land areas. *Int. J. Climatol.* **25,** 1965-1978 (2005).

55. Prasad, A. M., Iverson, L. R. & Liaw, A. Newer classification and regression tree techniques: bagging and random forests for ecological prediction. *Ecosystems* **9,** 181-199 (2006).

56. Sellers, P., Berry, J., Collatz, G., Field, C. & Hall, F. Canopy reflectance, photosynthesis, and transpiration. III. A reanalysis using improved leaf models and a new canopy integration scheme. *Remote Sens. Environ.* **42,** 187-216 (1992).

57. Ruimy A, Kergoat L, Bondeau A, Comparing global models of terrestrial net primary productivity (NPP): Analysis of differences in light absorption and light−use efficiency. *Glob. Change Biol.*, **5,** 56-64 (1999).

58. Yuan W, *et al.* Global comparison of light use efficiency models for simulating terrestrial vegetation gross primary production based on the LaThuile database. *Agric. For. Meteorol.* **192,** 108-120 (2014).

59. Wu, T. A mass-flux cumulus parameterization scheme for large-scale models: Description and test with observations. *Clim. Dyn.* **38,** 725-744 (2012).

60. Arora, V. *et al.* Carbon emission limits required to satisfy future representative concentration pathways of greenhouse gases. *Geophys. Res. Lett.* **38,** 5805 (2011).

61. von Salzen, K. *et al.* The Canadian fourth generation atmospheric global climate model (CanAM4). Part I: representation of physical processes. *Atmos. Ocean* **51,** 104-125 (2013).

62. Gent, P. R. *et al.* The community climate system model version 4. *J. Clim.* **24,** 4973-4991

(2011).

63. Long, M. C., Lindsay, K., Peacock, S., Moore, J. K. & Doney, S. C. Twentieth-century oceanic carbon uptake and storage in CESM1 (BGC). *J. Clim.* **26,** 6775-6800 (2013).

64. Hurrell, J. *et al.* The community earth system model: a framework for collaborative research, *Bull. Am. Meteorol. Soc.* **94,** 1339–1360 (2013).

65. Dunne, J. P. *et al.* GFDL's ESM2 global coupled climate-carbon Earth System Models. Part I: Physical formulation and baseline simulation characteristics. *J. Clim.* **25,** 6646-6665 (2012).

66. Dunne, J. P. *et al.* GFDL's ESM2 global coupled climate–Carbon Earth System Models. Part II: Carbon system formulation and baseline simulation characteristics. *J. Clim.* **26,** 2247-2267 (2013).

67. Volodin, E., Dianskii, N. & Gusev, A. Simulating present-day climate with the INMCM4.0 coupled model of the atmospheric and oceanic general circulations. *Izvestiya. Atmos. Ocean. Phys.* **46,** 414-431 (2010).

68. Hourdin, F. *et al.* Impact of the LMDZ atmospheric grid configuration on the climate and sensitivity of the IPSL-CM5A coupled model. *Clim. Dyn.* **40,** 2167-2192 (2013).

69. Watanabe, S. *et al.* MIROC-ESM: model description and basic results of CMIP5-20c3m experiments. *Geosci. Model Dev. Discuss.* **4,** 1063-1128 (2011).

70. Yukimoto, S. *et al.* A new global climate model of the Meteorological Research Institute: MRI-CGCM3: model description and basic performance. *J. Meteorol. Soc. Jpn.* **90,** 23-64 (2012).

71. Iversen, T. *et al.* The Norwegian earth system model, NorESM1-M—Part 2: climate

response and scenario projections. *Geosci. Model Dev.* **6,** 389-415 (2013).

72. Bentsen, M. *et al.* The Norwegian earth system model, NorESM1-M—Part 1: description and basic evaluation of the physical climate. *Geosci. Model Dev.* **6,** 687-720 (2013).

73. Nizinski, J., Galat, G. & Galat-Luong, A. Water balance and sustainability of eucalyptus plantations in the Kouilou basin (Congo-Brazzaville). *Russ. J. Ecol.* **42,** 305-314 (2011).

74. Frangi, J. L. & Lugo, A. E. Ecosystem dynamics of a subtropical floodplain forest. *Ecol. Monogr.* **55,** 351-369 (1985).

75. Paço, T. A. *et al.* Evapotranspiration from a Mediterranean evergreen oak savannah: the role of trees and pasture. *J. Hydrol.* **369,** 98-106 (2009).

76. Gibson, J. & Edwards, T. Regional water balance trends and evaporation -transpiration partitioning from a stable isotope survey of lakes in northern Canada. *Global Biogeochem. Cycles* **16,** doi:10.1029/2001GB001839 (2002).

77. Telmer, K. & Veizer, J. Isotopic constraints on the transpiration, evaporation, energy, and gross primary production budgets of a large boreal watershed: Ottawa River basin, Canada. *Global Biogeochem. Cycles* **14,** 149-165 (2000).

78. Hsieh, J. C., Chadwick, O. A., Kelly, E. F. & Savin, S. M. Oxygen isotopic composition of soil water: quantifying evaporation and transpiration. *Geoderma* **82,** 269-293 (1998).

79. Ferretti, D. *et al.* Partitioning evapotranspiration fluxes from a Colorado grassland using stable isotopes: seasonal variations and ecosystem implications of elevated atmospheric CO_2. *Plant Soil* **254,** 291-303 (2003).

80. Schlesinger, W. H. & Jasechko, S. Transpiration in the global water cycle. *Agric. For. Meteorol.* **189-190,** 115-117 (2014).

81. Lee, D., Kim, J., Lee, K.-S. & Kim, S. Partitioning of catchment water budget and its implications for ecosystem carbon exchange. *Biogeosciences* **7,** 1903-1914 (2010).

82. Zhao, W. et al. Evapotranspiration partitioning, stomatal conductance, and components of the water balance: A special case of a desert ecosystem in China. *J. Hydrol.* **538,** 374-386, (2016).

83. Liu, R., Li, Y. & Wang, Q. X. Variations in water and CO_2 fluxes over a saline desert in western China. *Hydrol. Process.* **26,** 513-522 (2012).

84. Mitchell, P. J., Veneklaas, E., Lambers, H. & Burgess, S. S. O. Partitioning of evapotranspiration in a semi-arid eucalypt woodland in south-western Australia. *Agric. For. Meteorol.* **149,** 25-37 (2009).

85. Granier, A., Biron, P. & Lemoine, D. Water balance, transpiration and canopy conductance in two beech stands. *Agric. For. Meteorol.* **100,** 291-308 (2000).

86. Dugas, W. A., Hicks, R. A. & Gibbens, R. P. Structure and function of C3 and C4 Chihuahuan Desert plant communities. Energy balance components. *J. Arid Environ.* **34,** 63-79 (1996).

87. Wilson, K. B., Hanson, P. J., Mulholland, P. J., Baldocchi, D. D. & Wullschleger, S. D. A comparison of methods for determining forest evapotranspiration and its components: sap-flow, soil water budget, eddy covariance and catchment water balance. *Agric. For. Meteorol.* **106,** 153-168 (2001).

88. Raz-Yaseef, N., Yakir, D., Schiller, G. & Cohen, S. Dynamics of evapotranspiration partitioning in a semi-arid forest as affected by temporal rainfall patterns. *Agric. For. Meteorol.* **157,** 77-85 (2012).

89. Liu, X. *et al.* Partitioning evapotranspiration in an intact forested watershed in southern China. *Ecohydrol.* **8,** 1037-1047 (2015).

90. Zhou, G.-Y. *et al.* Measured sap flow and estimated evapotranspiration of tropical Eucalyptus urophylla plantations in south China. *Acta Bot. Sin.* **46,** 202-210 (2004).

91. Sulman, B. N., Roman, D. T., Scanlon, T. M., Wang, L. & Novick, K. A. Comparing methods for partitioning a decade of carbon dioxide and water vapor fluxes in a temperate forest. *Agric. For. Meteorol.* **226,** 229-245 (2016).

92. Soubie, R., Heinesch, B., Granier, A., Aubinet, M. & Vincke, C. Evapotranspiration assessment of a mixed temperate forest by four methods: Eddy covariance, soil water budget, analytical and model. *Agric. For. Meteorol.* **228,** 191-204 (2016).

93. Qiu, G. Y., Li, C. & Yan, C. Characteristics of soil evaporation, plant transpiration and water budget of Nitraria dune in the arid Northwest China. *Agric. For. Meteorol.* **203,** 107-117 (2015).

94. Liu, X. *et al.* Partitioning evapotranspiration in an intact forested watershed in southern China. *Ecohydrol.* **8,** 1037-1047 (2015).

95. Bachand, P., Bachand, S., Fleck, J., Anderson, F. & Windham-Myers, L. Differentiating transpiration from evaporation in seasonal agricultural wetlands and the link to advective fluxes in the root zone. *Sci. Total Environ.* **484,** 232-248 (2014).

96. Domec, J.-C. *et al.* A comparison of three methods to estimate evapotranspiration in two contrasting loblolly pine plantations: age-related changes in water use and drought sensitivity of evapotranspiration components. *For. Sci.* **58,** 497-512 (2012).

97. Flumignan, D. L., de Faria, R. T. & Prete, C. E. C. Evapotranspiration components and

dual crop coefficients of coffee trees during crop production. *Agric. Water Manage.* **98,** 791-800 (2011).

98. Stoy, P. C. *et al.* Separating the effects of climate and vegetation on evapotranspiration along a successional chronosequence in the southeastern US. *Glob. Change Biol.* **12,** 2115-2135 (2006).

99. Oishi, A. C., Oren, R. & Stoy, P. C. Estimating components of forest evapotranspiration: a footprint approach for scaling sap flux measurements. *Agric. For. Meteorol.* **148,** 1719-1732 (2008).

100. Roupsard, O. *et al.* Partitioning energy and evapo-transpiration above and below a tropical palm canopy. *Agric. For. Meteorol.* **139,** 252-268 (2006).

101. Robertson, J. A. & Gazis, C. A. An oxygen isotope study of seasonal trends in soil water fluxes at two sites along a climate gradient in Washington state (USA). *J. Hydrol.* **328,** 375-387 (2006).

102. Iida, S. I., Tanaka, T. & Sugita, M. Change of evapotranspiration components due to the succession from Japanese red pine to evergreen oak. *J. Hydrol.* **326,** 166-180 (2006).

103. Kurpius, M., Panek, J., Nikolov, N., McKay, M. & Goldstein, A. H. Partitioning of water flux in a Sierra Nevada ponderosa pine plantation. *Agric. For. Meteorol.* **117,** 173-192 (2003).

104. Black, T. *et al.* Annual cycles of water vapour and carbon dioxide fluxes in and above a boreal aspen forest. *Glob. Change Boil.* **2,** 219-229 (1996).

105. Daikoku, K. *et al.* Influence of evaporation from the forest floor on evapotranspiration from the dry canopy. *Hydrol. Process.* **22,** 4083-4096 (2008).

Table S1. CMIP5 ESM details. Information about 19 CMIP5 ESMs used in this study and their associated land surface models.

				Model Information			
Institute	**Nation**	**Modeling Center**	**Reference**	**Model Name**	**Resolution**	**Coupled Land Surface Model**	**RCP8.5 Availability**
BCC	China	Beijing Climate Center, China Meteorological Administration	59	bcc-csm1-1	2.8125°×2.8125°	BCC AVIM1.0	yes
				bcc-csm1-1-m	1.125°×1.125°	BCC AVIM1.0	yes
CCCma	Canada	Canadian Centre for Climate Modeling and Analysis	60, 61	CanESM2	2.8125°×2.8125°	CLASS2.7 & CTEM1	yes
NCAR	USA	National Center for Atmospheric Research	62	CCSM4	0.9°×1.25°	CLM4	yes
NSF-DOE-NCAR	USA	Community Earth System Model Contributors	63 64	CESM1-BGC	0.9°×1.25°	CLM4	yes
				CESM1-CAM5	0.9°×1.25°	CLM4	yes
				CESM1-FASTC	0.9°×1.25°	CLM4	no

				HEM			
				CESM1-WACCM		CLM4	yes
GFDL	USA	NOAA Geophysical Fluid Dynamics Laboratory	65, 66	GFDL-ESM2M	2°×2.5°	LM3	yes
				GFDL-ESM2G	2°×2.5°	LM3	yes
INM	Russia	Institute for Numerical Mathematics	67	inmcm4	1.5°×2°	Simple model	yes
IPSL	France	Institute Pierre-Simon Laplace	68	IPSL-CM5A-LR	1.89°×3.75°	ORCHIDEE	yes
				IPSL-CM5A-MR	1.89°×3.75°	ORCHIDEE	yes
MIROC	Japan	National Institute for Environmental Studies, The University of Tokyo	69	MIROC-ESM	2.8125°×2.8125°	MATSIRO	yes
				MIROC-ESM-CHEM	2.8125°×2.8125°	MATSIRO	yes
				MIROC4h	0.5625°×0.5625°	MATSIRO	no

				MIROC5	1.40625°×1.40625°	MATSIRO	no
MRI	Japan	Meteorological Research Institute	70	MRI-ESM1	1.125°×1.125°	HAL	yes
NCC	Norway	Norwegian Climate Centre	71, 72	NorESM1-M	1.875°×3 2.5°	CLM4	yes

Table S2. Available field observations. Characteristics, locations and temporal availability of in situ observations of T/ET compiled from stand-based studies available in the literature. Asterisks indicate those sites located on small islands which cannot be represented in GCMs due to computational limitations.

Number	Ecoregion	Country	Latitude	Longitude	Location
1	Tropical Rainforest	D.R. Congo	-4.7	12.1	Pointe–Noire
2	Tropical Rainforest	Puerto Rico	18.3	-65.7	Luquillo Experimental Forest
3	Temperate Deciduous Forests	Portugal	38.5	-8.0	Herdade da Alfarrobeira
4	Boreal Forest	Canada	63.4	-114.3	Northwest Territories and Nunavut
5	Boreal Forest	Canada	45.7	-76.9	Ottawa River basin
6	Tundra	Canada	64.5	-112.7	Northwest Territories and Nunavut
7	Tropical Grassland	USA	20.1	-155.8	Kohala, Hawaii
8	Temperate Grassland	USA	40.7	-104.8	Colorado: Central Plains Experimental Range
9	Desert	USA	32.5	-106.8	Jornada Experimental Range
10	Temperate Forest	Korea	37.0	128.0	The Han River Basin
11	Shrubland Desert	China	39.4	100.1	Loess Plateau
12	Desert	China	44.3	87.9	Gubantonggut Desert: Fukang Station of Desert Ecology
13	Temperate Deciduous Forests	Australia	-32.3	117.9	Corrigin, Western Australia
14	Temperate Deciduous Forests	France	48.7	7.1	Hesse
15	Grassland	New Mexico	32.3	106.8	Jornada Experimental Range

16	Deciduous Forest	USA	36.0	-84.3	Walker Branch Watershed
17	Forest	Israel	31.4	35.0	The edge of the Judean Mountain ridge
18	Evergreen Forest	China	23.2	112.5	The Dinghushan Biosphere Reserve
19	Tropical Forest	China	21.0	109.9	Hetou and Jijia at Leizhou Peninsula
20	Temperate Deciduous Forest	USA	39.3	-86.4	Monroe State Forest in south-central Indiana
21	Mixed Forest	Belgium	50.3	6.0	Vielsalm in a Belgian Ardennes forest
22	Shrubland	China	38.6	103.5	Minqin, Shiyang River, Gansu Province
23	Evergreen Broadleaf Forests	China	23.2	112.5	The Dinghushan Biosphere Reserve
24	Croplands	USA	38.6	-121.6	The Yolo Bypass at the Sacramento River watershed
25	Mixed forests	USA	35.8	-76.7	North Carolina
26	Croplands	Brazil	-23.3	-51.2	the Instituto Agronômico do Paraná (IAPAR), in Londrina, Paraná State
27	Broadleaf Deciduous forests	USA	36.0	-79.1	the Blackwood Division of the Duke Forest
28	Broadleaf Deciduous forests	USA	37.0	-79.1	A oak-hickory forest in North Carolina
29	Tropical Cropland	Vanuatu	-15.4	167.2	the Vanuatu Agricultural Research and Technical Centre
30	Shrub-steppe	USA	46.9	-127.5	Ellensburg on the eastern side of the Cascade Mountains
31	Coniferous forest	USA	47.2	-120.9	Cle Elum on the eastern side of the Cascade Mountains
32	Evergreen Broadleaf Forests	Japan	36.1	140.1	Adjacent to University of Tsukuba

33	Temperature Forest	USA	38.9	-120.6	A ponderosa pine plantation in the Sierra Nevada Mountains
34	Boreal Forests	Canada	53.7	-106.2	The Prince Albert National Park
35	Mixed Forest	Japan	35.3	137.1	Seto National Forest, Aichi

Number	Period of Measurement	Method	Annual mean PRE (mm)	Annual mean TMP (^{o}C)
1	Feb 1997 - Jul 1999	Radial flow meter, Water balance equation	1188	24.9
2	Apr 1980 - May 1981	Diurnal water table changes	3727	19.7
3	2001 - 2006	Sap flow	669	15
4	1993 - 1994	Isotope-based	400	-10
5	Sep 1991 - Sep 1992	Isotope-based	872	3.5
6	1993 - 1994	Isotope-based	400	-10
7	Dec 1993 - Nov 1994	Isotope-based	-	-
8	2000 - 2001	Isotope-based	320	8.1
9	Jun 1983 - Jun 1984	Water-balance; control and bare plots	-	-
10	Dec 2004 - Jun 2006	Isotope-based	1244	11
11	2008 - 2010	Sap flow	116.8	7.6
12	Jan - Dec 2009	Micro-lysimeters, Eddy Covariance	173	6.5
13	Nov 2005 - May 2007	Sap flow	265	-
14	Jun 1996 - Dec 1997	Sap flow	820	9.2
15	1991 - 1992	-	241	24.5
16	Jan - Dec 1998	Sap Flow, Eddy Covariance	1333	14.4
17	Oct 2004 - May 2007	Chamber, Micro-lysimeters	285	17.5
18	2003 - 2011 for ET,	Sap Flow,	1678	20.9

	Jul 2010 - Jun 2011 for T	Eddy Covariance		
19	Sep 1999 - Sep 2000	Sap Flow, Eddy Covariance	1900	22
20	Jan 2004 - Dec 2013	Flux-variance Similarity, Eddy Covariance	-	-
21	2010 - 2011	Eddy Covariance, Sap flow Measurements	-	-
22	May 2010 - June 2012	Bowen ratio energy balance and water balance, Thermal infrared remote sensing	110	7.8
23	2003 - 2011 for ET, July 2010 to June 2011 for T	Eddy Covariance, Sap flow Probes	1678	20.9
24	2000/2001 - 2009/2010 (July - June)	Hydrologic and tracer mass budgets	420	-
25	2007 - 2009	Eddy Covariance, Sap flow Probes	1308	15.5
26	Sep 2004 - Aug 2006	Weighing lysimeters, micro-lysimeters	1500	21.5
27	2002 - 2005	Eddy covariance-generated estimates	1145	15.5
28	2002 - 2005	Eddy Covariance, Sap flow Probes	1146	13.2
29	Oct 2001 - Sep 2004	Eddy-covariance, Sap flow	-	-
30	Jul 2000 - May 2001	Isotope-based (stand level)	225	8.7
31		stable isotopes	564	8.1
32	Aug 2001 - Jul 2002	Energy balance equation, Sap flow	1207	14.1
33	Jun 2000 - May 2001	Eddy-covariance, Sap flow	1630	12.5
34	Oct 1993 - Sep 1994	Eddy correlation method, lysimeters	458	-
35	Aug 2005 - Aug 2006	Chamber, lysimeters,	1460	-

Eddy-covariance

Number	Match with MODIS	T/ET(%)	1 SD (%)	Reference
1	yes	85.50	2.12	73
	yes	61.44	0.76	74
3	yes	76.54	3.19	75
4	yes	81.40	5.89	76
5	yes	85	-	77
6	no	74.07	10.76	76
7	-	56*	16.99	78
8	yes	60	9.02	79
9	no	72	-	80
10	yes	47.22	1.39	81
11	yes	76.35	1.79	82
12	no	38	-	83
13	no	40	5.62	84
14	yes	69	-	85
15	no	45	7.35	86
16	yes	43.13	2.47	87
17	no	48.78	5.90	88
18	yes	60.20	5.49	89
19	no	56.75	7.70	90
20	no	82	-	91
21	no	58.50	3.56	92
22	yes	68.50	23.3	93
23	yes	60.20	5.2	94
24	yes	64.50	13.44	95
25	yes	77.03	6.635	96

26	yes	65	5.82	97
27	yes	71.64	0.647	98
28	no	56.04	2.09	99
29	yes	68*	4.46	100
30	yes	74.97	-	101
31	yes	60.13	-	102
32	yes	67.17	8.01	103
33	yes	58.14	32.93	104
34	no	70.97	-	105
35	yes	73.33	-	106

Table S3. Environmental drivers. Description and units of environmental variables used in this study. Asterisks denote that the corresponding variables are directly from the model output. In particular, 10-meter wind speed (WS) for CCSM4, CESM1-BGC, CESM1-CAM5, CESM1-FASTCHEM and CESM1-WACCM is extrapolated from the wind speed at the closest pressure level based on a power-law velocity profile equation.

Abbreviation	Name	Relating output variables (CMIP5 protocol name)	Unit	Calculation
T	Plant transpiration Flux	trans	$mm\ yr^{-1}$	*
ET	Evapotranspiration Flux	evspsbl	$mm\ yr^{-1}$	*
LAI	Leaf Area Index	lai	$m^2\ m^{-2}$	*
TAVG	Daily Average Temperature	tas	K	*
DTR	Diurnal Temperature Range	tasmax, tasmin	K	tasmax - tasmin
PRE	Precipitation	pr	$mm\ yr^{-1}$	*
VPD	Vapor Pressure Deficit	tas, ps, hurs	kPa	see Methods
RN	Net Solar Radiation	rsus, rsds, rlds, rlus	$w\ m^{-2}$	(rsds + rlds) - (rsus + rlus)
SWC	Soil Water Content	mrso	$mm\ yr^{-2}$	*
TMX	Daily Maximum Temperature	tasmax	K	*
TMN	Daily Minimum Temperature	tasmin	K	*
WS	10-m Wind Speed	uas, vas ua, va	$m\ s^{-1}$	$\sqrt{uas^2 + vas^2}$

PS	Surface Air Pressure	ps	kPa	*
RH	Relative Humidity	hurs	%	*
LST	Land Surface Temperature	ts	K	*
CLD	Cloud Area Fraction	clt	%	*
GPP	Gross Primary Production	gpp	$kg\ m^{-2}\ yr^{-}$	*

Table S4. Best-fit values for the "big-leaf" model emulating ESMs. Inferred values of τ and A_0 based on an adjusted big-leaf model, with optimum parameters minimize differences between predicted T/ET values from the big-leaf model and CMIP5-derived T/ET values across the LAI gradients (Fig. 3b). Inferred LUE values using the optimized τ and model outputs of LAI and GPP are also listed.

Model Name	τ	A_0 ($\mu mol\ m^{-2}\ s^{-1}$)	**RMSE**	**LUE** ($g\ C\ m^{-2}\ MJ^{-1} APAR$)
CCSM4	0.25	1.21	0.03	1.08
CESM1-BGC	0.25	1.21	0.03	1.07
CESM1-CAM5	0.28	1.31	0.02	1.06
CESM1-FASTCHEM	0.24	1.17	0.03	1.09
CESM1-WACCM	0.25	1.42	0.02	1.14
CanESM2	0.75	4.26	0.01	0.79
GFDL-ESM2G	0.77	5.49	0.05	0.94
GFDL-ESM2M	0.48	3.49	0.05	1.11
IPSL-CM5A-LR	0.62	3.91	0.04	0.78
IPSL-CM5A-MR	0.66	3.93	0.04	0.76
MIROC-ESM	0.63	2.76	0.06	0.52
MIROC-ESM-CHEM	0.57	2.60	0.05	0.55
MRI-ESM1	0.62	6.56	0.03	1.25
NorESM1-M	0.21	1.16	0.03	1.29
bcc-csm1-1	0.64	2.91	0.02	0.54
bcc-csm1-1-m	0.53	1.96	0.02	0.58
inmcm4	0.76	4.91	0.04	0.65

Figure S1. Sensitivity of constrained global T/ET to the number of used sites. Global T/ET values constrained by a subset (ranging from 1 to 33) of randomly selected site observations. Error bars indicate the 1-SD of the 100 repeated experiments for each site amount.

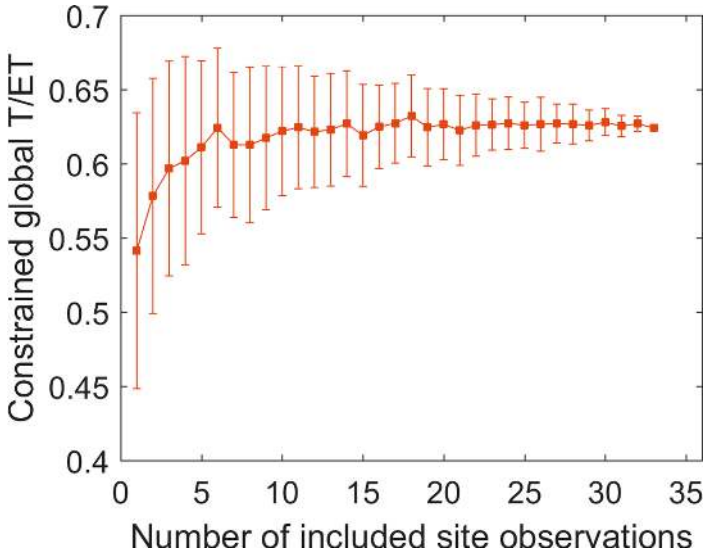

Figure S2. Same as Fig. 2, but averaging climatically analogue model grid cells to replace the location-specified model grid cell.

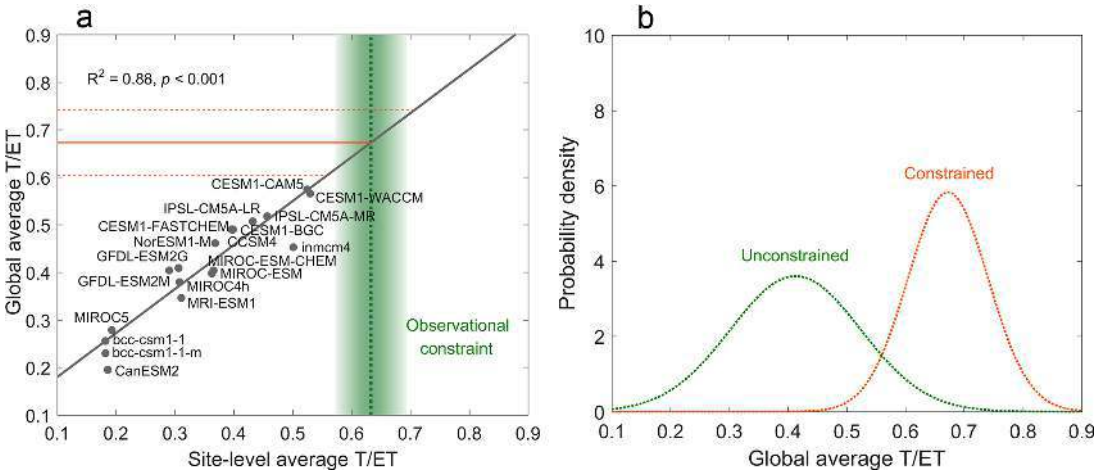

Figure S3. Same as Fig. 2, but only using 22 sites where their vegetation type can represent dominant vegetation type of the corresponding pixels.

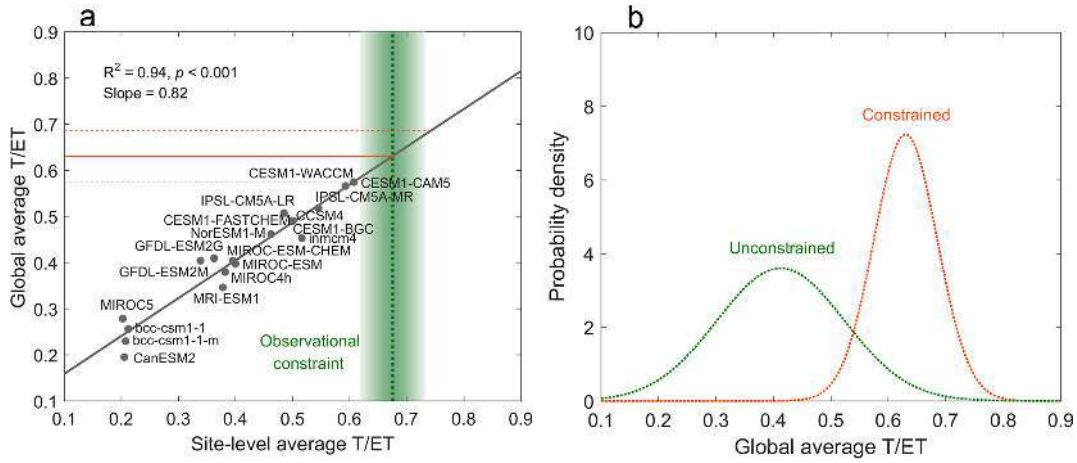

Figure S4. Same as Fig. 2, but using the isotope-based observations (a, c) and non-isotope-based observations (b, d), respectively, to constrain the global T/ET value. T/ET values measured by isotopic approaches is considerably higher than that measured by other approaches, such as the combination of sap-flow and eddy covariance[7,11]. This is because some assumptions underlying this approach (e.g., the isotopic steady state of non-fractionating transpiration vs. fractionating evaporation) are rarely met perfectly in nature[11]. As a result, the constrained T/ET with isotopic observations (0.71 ± 0.07) is higher than that with the non-isotopic observations (0.61 ± 0.06). Nevertheless, the two constrained T/ET values are both higher than ESM simulation results.

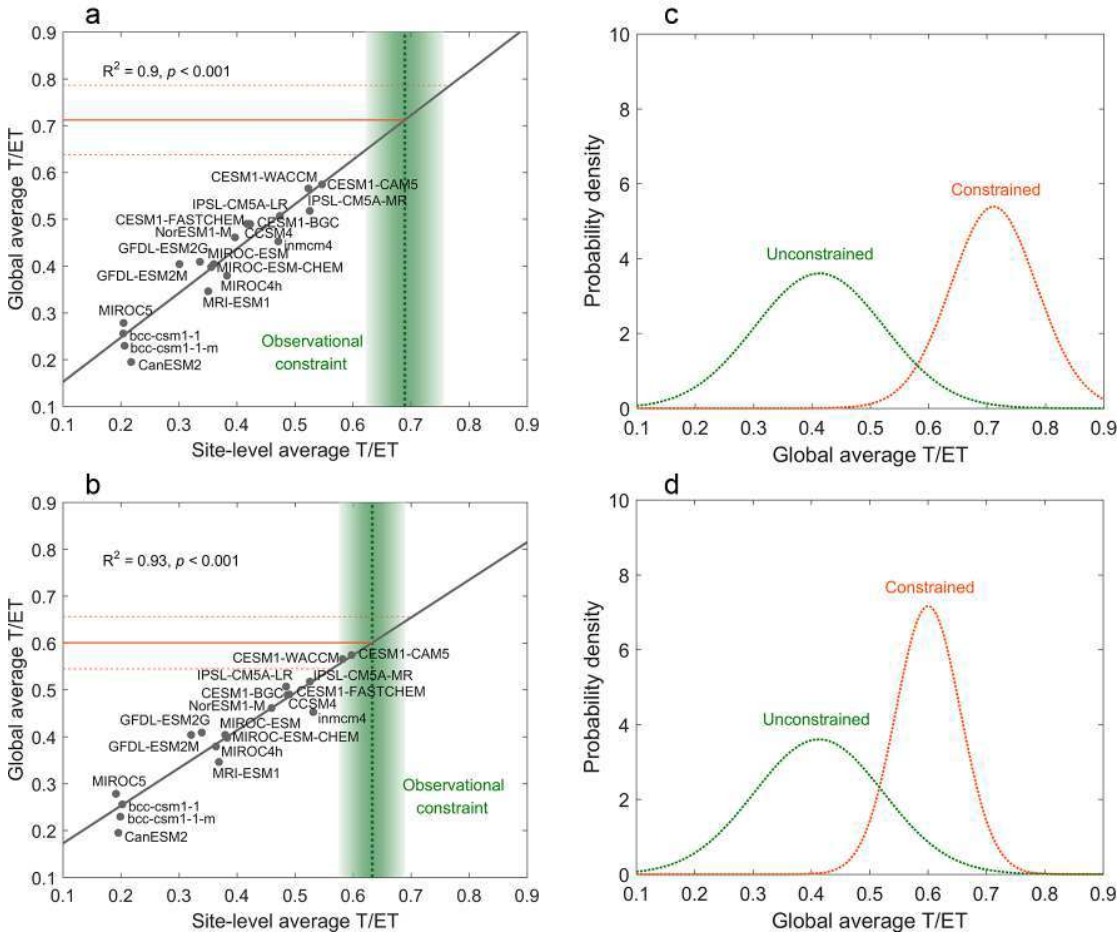

Figure S5. ESM-based meteorological drivers, and their replacement in BRT model with measurements. a, Comparison between model-derived global mean of environmental variables (DTR, TMX, SWC, PRE and RN) and corresponding observations/climate reanalysis (horizontal bars). **b**–**d**, Scatterplots of CMIP5 modeled T/ET versus BRT-modeled T/ET, but with temperature (DTR and TMX), water availability (SWC and PRE), and radiation (RN) replaced by corresponding observations/climate reanalysis, respectively. Legend for ESMs common in all panels.

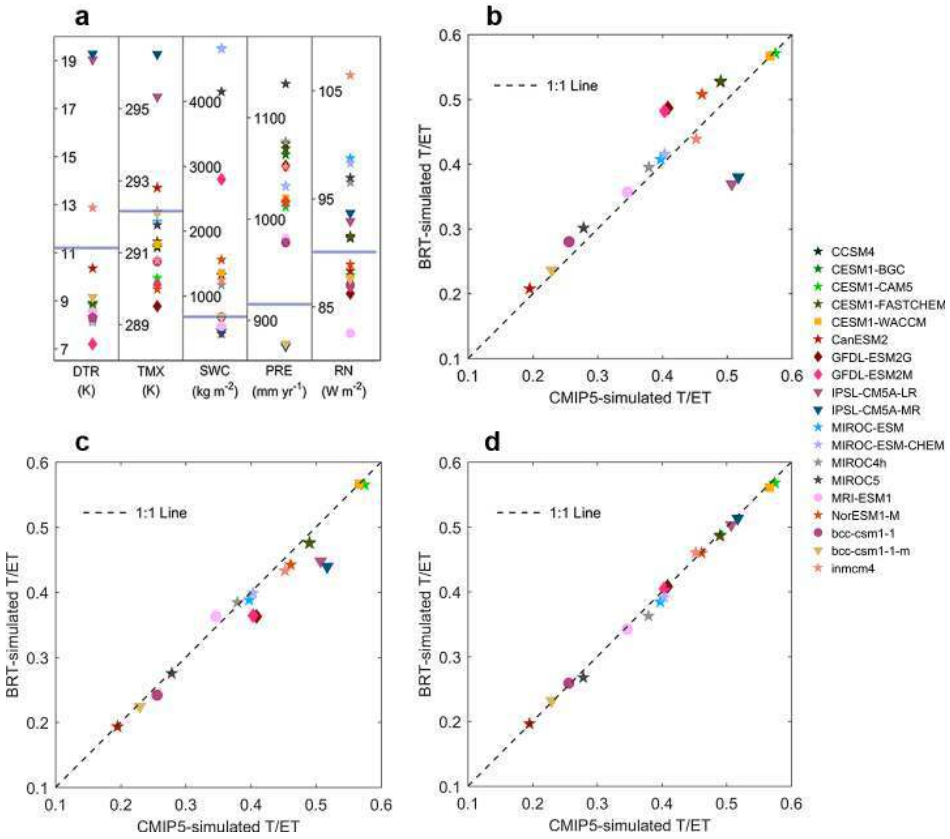

Figure S6. **Inferred implications for T/ET through τ changes**. **a**, Variations in the T/ET ratio in response to variations in light extinction coefficient ($0.2 \leq \tau \leq$ the fitting value) for each ESM. **b**, The increase in T/ET values when driven by a lower τ (0.2, 0.3 and 0.4) compared to the best-fitted τ for each ESM.

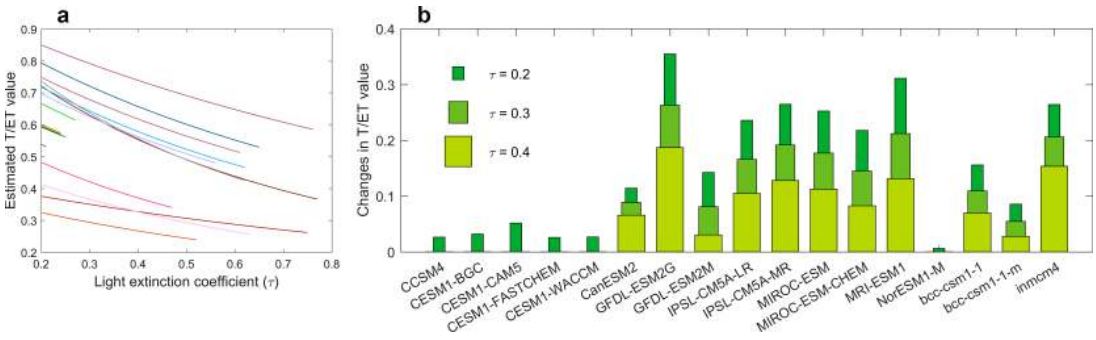

Figure S7. **Impact of interception loss on global T/ET ratio.** Modelled global average T/ET versus simulated **a**) global average interception loss and **b**) global average interception ratio (defined as the ratio of interception loss to total precipitation). This is across 19 CMIP5 ensemble members, as marked. The dark gray line indicates the best-fit regression line across the CMIP5 models. The red solid line and dashed lines represents respectively the observation-based value[39] and its uncertainty bounds of interception loss (or interception ratio). This global interception estimate is derived from the satellite-based assimilating data using the Gash's analytical model[39].